Title:

Hybrid broadband ground-motion simulation using neural networks with spatial, inter-period, and cross-component correlations

Authors:

Victor M. Hernández-Aguirre[1]

Rajesh Rupakhety[1]

Roberto Paolucci[2]

Manuela Vanini[2]

Chiara Smerzini[2]

[1] Earthquake Engineering Research Centre, Faculty of Civil and Environmental Engineering, University of Iceland, Austurvegur 2a, 800 Selfoss, Iceland

Email: victorh@hi.is

[2] Department of Civil and Environmental Engineering, Politecnico di Milano, Milan, Italy

Date of Preprint Posting:

9 March 2026

Hybrid broadband ground-motion simulation using neural networks with spatial, inter-period, and cross-component correlations

Victor M. Hernández-Aguirre[1] · **Rajesh Rupakhety**[1] · **Roberto Paolucci**[2] · **Manuela Vanini**[2] · **Chiara Smerzini**[2]

Abstract: Simulated ground motions are increasingly used in earthquake engineering, particularly in regions with sparse strong-motion recordings where constraining non-ergodic ground-motion models (GMMs) remains challenging. Physics-based simulations (PBS) can reproduce key source and wave-propagation effects but are often limited to low frequencies, whereas stochastic methods are computationally efficient but typically lack physically coherent three-component behaviour and realistic near-fault features. Here we develop a hybrid broadband framework with three main innovations (i) an enhanced artificial neural network (ANN) that predicts short-period spectral accelerations (SAs) from long-period PBS SAs and scalar source-site predictor variables, while jointly modelling the three ground-motion components, (ii) a transfer learning strategy that enables regional calibration in data-limited settings, and (iii) an explicit multivariate correlation model for within-event residuals that restores realistic broadband dependence jointly across space, periods, and components. The approach is validated using regional 3D PBS of the Mw 6.5 and Mw 6.4 June 2000 South Iceland earthquakes. The resulting broadband fields reproduce observed short-period attenuation and near-fault saturation, match the local Icelandic GMM trends, and preserve physically plausible directionality and component ratios, including spatially varying FN/FP patterns and V/H ratios consistent with empirical models. Inter-period correlations of within-event residuals follow established empirical trends and, importantly, remain continuous across the stochastic–PBS transition, while spatial correlation ranges are comparable to published observations. Owing to its computational efficiency, the framework is well suited for seismic hazard and risk applications that require spatially and spectrally coherent broadband ground motions in dense spatial grids.

Keywords: Physics-based numerical simulations; machine learning; transfer-learning; broadband ground-motion simulation; ground-motion correlation.

1 Introduction

Simulated ground motions have become increasingly important in earthquake engineering practice, particularly in regions with sparse instrumental strong-motion records or limited coverage of near-fault observations. In such settings, constraining non-ergodic ground-motion models (GMMs), especially in the near field and for large magnitudes, remains challenging. Ground-motion simulation approaches are commonly classified into three categories: deterministic, stochastic, and hybrid.

Deterministic approaches, often referred to as physics-based simulations (PBS), solve the elastodynamic equations to model seismic wave propagation from the source to the site of interest. PBS can reproduce key physical phenomena such as near-fault directivity and the effects of topography and complex site conditions. However, their computational cost and the difficulty of accurately characterizing source complexity and 3-D regional structure often limit their ability to reproduce high-frequency ground-motion content. Consequently, PBS are frequently applied up to about 2–3 Hz, although successful applications extending to ~8 Hz have been reported [1–3]. This can constrain their use in earthquake engineering applications, such as structural analyses and risk assessment studies, that typically require realistic ground-motion characteristics up to about 10 Hz.

Stochastic simulation methods, have their basis in the work of Hanks and McGuire [4], who combined seismological models of the spectral amplitude of ground motion with the engineering notion that high-frequency motions are essentially random. Finite-fault implementations are widely used for simulating large-magnitude events, typically by subdividing the fault into sub-sources and summing their contributions with appropriate time delays [5]. Each sub-source is modelled as a point-source producing a signal represented by band-limited white Gaussian noise shaped by source, path, and site effects [6]. Although stochastic methods are computationally efficient, they exhibit limitations, notably in capturing directivity and in producing physically coherent three-component seismograms [7].

Hybrid methods leverage the strengths of physics-based low-frequency (LF) simulations and extend their frequency content by merging LF ground motions with high-frequency components generated using computationally efficient techniques. Examples include using stochastic ground motions [8], scatterograms based on the multiple S-to-S scattering theory [9,10], Green's functions computed using 1D models with a site-effect correction [11], and machine-learning approaches [12–14].

Earthquake recordings show that ground-motion intensity measures exhibit both spatial correlation and inter-period (inter-frequency) correlation. Over the past decades, numerous studies have investigated the spatial correlation of response spectra [15–18], as well as inter-period correlations in response spectra and inter-frequency correlations in Fourier spectra [19–24]. Several works have also shown that neglecting these correlations can bias risk estimates, typically leading to an underestimation of seismic risk [22,25–27]. Although PBS inherently include realistic spatial correlation of LF motion arising from source and path effects [28,29], many stochastic and hybrid simulation methods do not provide realistic broadband (BB) spatial and/or inter-period correlation, or exhibit artificial loss of correlation near the LF–HF transition [30]. This limitation is particularly relevant when simulated motions are used as inputs to portfolio risk, spatially distributed infrastructure assessment, or multi-period vector-valued engineering demand models.

The objective of this work is threefold. First, we develop and validate an enhanced version of the ANN architecture proposed by Paolucci et al. [14] to predict short-period spectral accelerations (SAs) from long-period SAs obtained from PBS. More broadly, machine-learning (ML) methods have increasingly supported seismology by improving ground-motion prediction, early-warning performance, earthquake catalogue development, and other data-driven seismic analyses [31]. Second, leveraging transfer learning (TL) [32] allows the proposed ML workflow to be applied in regions with scarce strong-motion recordings: an ANN is first pretrained on a large global ground-motion dataset to learn robust magnitude–distance scaling and other transferable trends, and is then fine-tuned using a limited local dataset. Recent applications of TL in earthquake engineering include rapid prediction of ground-motion intensity measures [33] and the development of ground-motion models for data-limited [34]. Third, we develop an empirical multivariate correlation model for the within-event residuals of the ANN predictions, enabling the generation of spatially, spectrally, and cross-component correlated broadband ground-motion fields suitable for hazard and risk applications. These fields can be generated unconditionally for scenario-earthquake applications, or conditionally on observed ground motions, for example when reconstructing historical earthquakes.

The paper is structured as follows. We present the proposed ANN for estimated BB SA from PBS results, and then we show how this ML model can be trained even when only limited data is available. Then we discuss the modelling of spatial and cross-period/cross-component correlation of within-event residuals that can be jointly used with the ANN model. The methodology is then applied and validated using low-frequency PBS of South Iceland earthquakes [35], followed by a discussion of implications for engineering practice.

2 ANN to predict short-period spectral ordinates

2.1 ANN2BB method

Paolucci et al. [14] proposed a hybrid data-driven simulation framework, termed artificial neural network to broadband (ANN2BB), to generate BB ground motions by extending physics-based LF simulations with data-driven predictions of short-period response spectra. The core idea is that, for a given LF simulated ground motion, short-period spectral accelerations SA($T<T^*$) can be inferred from the long-period ordinates SA($T\geq T^*$) computed from PBS. This mapping is performed using two-hidden-layer feed-forward ANNs, trained with records separately for the geometric mean of the horizontal components (GMH) and for the vertical component SA. The resulting target spectrum is obtained by concatenating the predicted short-period ordinates with the simulated long-period ordinates, i.e., SA($T<T^*$) ∪ SA($T\geq T^*$). High-frequency (HF) time histories are then generated using the non-stationary stochastic method of Sabetta et al. [36], and the scaled realization whose response spectrum best matches the target spectrum is selected. Finally, the selected HF signal and the LF physics-based waveform, after applying complementary high- and low-pass filtering, respectively, are merged in the time domain to form a BB seismogram. The corner period T* (equivalently, the transition frequency) is chosen based on the maximum resolvable frequency of the physics-based simulation.

The ANN2BB methodology has been applied to a variety of earthquake scenarios spanning a broad range of magnitudes, faulting styles, and geological settings, which were compiled in the BB-SPEEDset database [37]. These BB simulations were shown to reproduce, in a statistical sense, peak values, integral intensity measures, durations, and attenuation trends consistent with recorded near-fault motions, as found from the NESS database [38]. Nevertheless, the original ANN2BB formulation exhibits several limitations that motivate the developments proposed in this study. First, the ANNs are trained using only long-period spectral accelerations as inputs. When residuals are examined as a function of Joyner–Boore distance (R_{JB}), this formulation can lead to systematic distance-dependent bias. This effect was not evident in [14] because residuals were analysed primarily as a function of period, for which no bias was observed. Second, for the horizontal components the ANN is trained on GMH, while the two horizontal components are subsequently generated independently. As a result, strong polarization present at long periods may be implicitly transferred into the predicted short-period ordinates, because the ANN acts purely as a mapping between spectral shapes without explicit control of cross-component behaviour. This is potentially problematic in the near field, where long-period ground motion is often strongly polarized due to rupture directivity and source radiation effects, but such polarization tends to diminish at higher frequencies, largely due to the combined influence of short-wavelength rupture heterogeneity and path scattering arising from small-scale velocity fluctuations [39,40]. These issues are addressed through an improved deep ANN architecture described in the following section.

2.2 Architecture of the ANN

Artificial neural networks are flexible, data-driven models designed to learn complex nonlinear relationships between input and output variables directly from examples [41,42]. Unlike closed-form empirical regressions, where functional forms and interaction terms must be specified a priori, ANNs can automatically capture coupled effects, nonlinearities, and variable interactions that are difficult to represent analytically, particularly when the mapping depends on many correlated predictors. From a functional perspective, feed-forward ANNs approximate the target relationship through a composition of affine transformations and nonlinear activation functions, and, under mild conditions, can approximate a broad class of continuous functions [43]. During training, network parameters are optimized to minimize a loss function that quantifies the mismatch between predicted and observed outputs, commonly using gradient-based algorithms [42], while techniques such as early stopping and dropout are often adopted to improve generalization [44]. This makes ANNs particularly suitable for broadband ground-motion prediction, where the relationship between components, and long-period and short-period spectral ordinates is strongly nonlinear and influenced by multiple coupled factors.

The proposed deep ANN architecture consists of six input branches (Figure 1). The first three correspond to the as recorded long-period spectral accelerations of the two horizontal components and the vertical component. The fourth branch includes scalar source and path parameters. Finally, the last three branches include EC8 site class (SC: A, B, C, or D), faulting mechanism (FM: normal - NF, reverse/thrust - TF or strike-slip - SS), and region (RG: Italy - IT, California - CA, Taiwan - TW, Türkiye - TR, Japan – JP, or Other – OT), respectively. These three branches are represented by a one-hot encoded vector, that for instance, it would be [1,0,0,0] for SC A, [0,0,1] for strike-slip FM, and [0,0,0,1,0,0] for Türkiye. Each input branch is first processed independently through fully connected layers, with hyperbolic tangent (tanh) activation functions for the first four layers, and rectified linear unit (ReLU) activation functions for the last three. Afterwards, they are merged via a concatenation layer, which is then passed to a fully connected hidden layer (common layer) with a tanh activation function. Processing these input groups through separate branches allows the network to learn distinct representations for spectral shape, scalar source–path effects, and categorical metadata before combining them, which improves training stability and interpretability compared to a single fully connected input layer.

Finally, this common layer connects to three separate output layers with linear activation functions, each predicting the short-period spectral accelerations of horizontal and vertical components. To ensure comparability across variables, z-score normalization is applied to the first four input branches. Input and output spectral accelerations are given in natural logarithmic scale ln(SA), with SA in m/s^2. For each component we use a total of 29 SAs for periods going from 0 to 5 sec. These 29 periods are divided into input/output depending on the corner period T*. For instance, for T*=1 s, the output periods are [0,0.05,0.07,(0.1:0.05:0.5),0.6,0.7,0.75,0.8,0.9 s].

With respect to the ANN proposed by [14], we augment the inputs with source, path, and site parameters commonly used in GMMs, as this has been shown to improve predictive performance in related ANNs [45]. A further and key distinction from existing ANN approaches for estimating short-period spectral ordinates [14,45,46] is that we model the three components simultaneously. Because the long-period spectral ordinates are provided as inputs, the network is implicitly conditioned on event- and path-specific effects embedded in the LF motion, such as rupture directivity, distance-dependent attenuation, and source characteristics that control spectral shape, thereby enabling a more event-specific mapping than would be possible using a GMM with only scalar metadata. In this sense, the proposed ML model can be interpreted as a data-driven, non-parametric generalized ground-motion prediction model [47], summarized as

$$\ln \mathbf{SA}(\mathbf{T} < \mathbf{T}^*)^{(\mathbf{H1,H2,V})} = \mathbf{f}_{\boldsymbol{\theta}}\left(\ln \mathbf{SA}(\mathbf{T} \geq \mathbf{T}^*)^{(\mathbf{H1,H2,V})}, \mathrm{M_w}, \mathrm{R_{JB}}, \ln\left(\mathrm{R_{JB}}\right), \mathrm{D_h}, \mathrm{SC}, \mathrm{FM}, \mathrm{RG}\right), \tag{1}$$

where $\mathbf{SA}(\mathbf{T} < \mathbf{T}^*)^{(\mathbf{H1,H2,V})}$ and $\mathbf{SA}(\mathbf{T} \geq \mathbf{T}^*)^{(\mathbf{H1,H2,V})}$ denote the stacked short- and long-period spectral accelerations for the two horizontal components and the vertical component, and $\mathbf{f}_{\boldsymbol{\theta}}$ is the trained ANN.

By jointly learning the mapping for the two horizontal and vertical components, the ANN can reproduce physically plausible cross-component dependence at short periods, while allowing to reproduce the ground motion polarization features at short periods, consistent with observed ground motion behaviour, which typically shows a decreasing trend as frequency increases

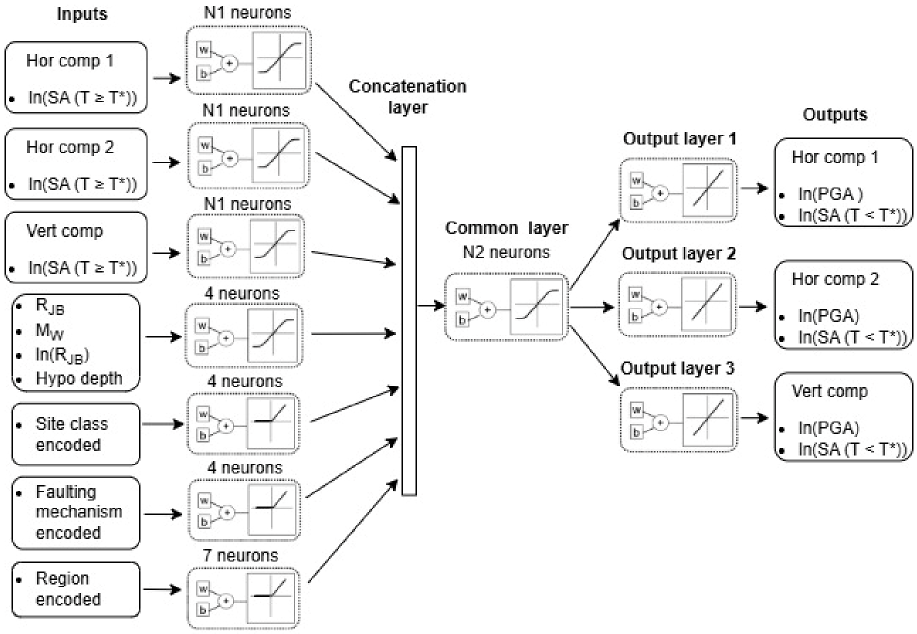

Figure 1. Architecture of the deep artificial neural network model to predict three-component short-period response spectra SA(T<T*) from long-period spectra SA(T≥T*), R_{JB} (Joyner-Boore distance), ln(R_{JB}), M_w, hypocentral depth (D_h), site class, faulting mechanism, and region.

2.3 Dataset and training

The training dataset combines records from earthquakes with $M_w \geq 5$ and $R_{JB} \leq 130$ km from the ESM database [48], together with records from earthquakes with $M_w \geq 6.5$ from the NGA-West2 database[49]. The combination of ESM and NGA-West2 data was adopted to ensure adequate coverage of both moderate-to-large magnitudes and near-fault distances, while maintaining sufficient diversity in tectonic setting, site conditions, and source characteristics to support robust ANN training. The combined dataset consists of a total of 5148 three-component strong-motion records from crustal earthquakes with hypocentral depths less than 30 km. Figure 2 shows the M_w vs R_{JB} distribution of the records used for training the model.

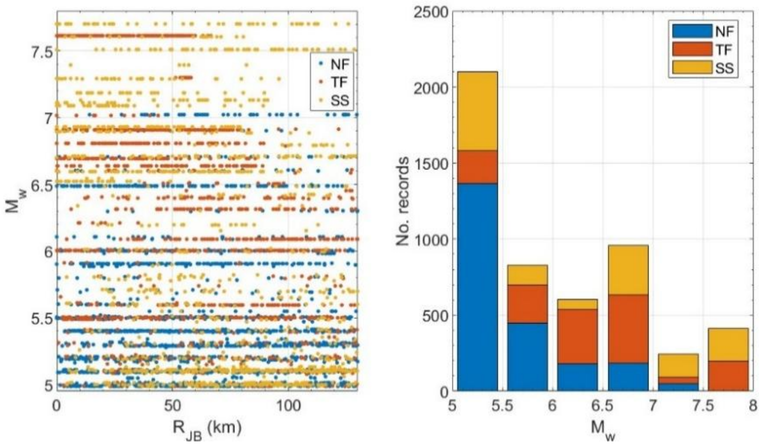

Figure 2. Magnitude M_w vs R_{JB} scatter plot of recordings in the ESM+NGA-West2 dataset used for training the ANN, including 5148 strong-motion records from crustal earthquakes (left). Points are color-coded by focal mechanism: NF (normal), TF (reverse/thrust), and SS (strike-slip). Histogram of the number of events per magnitude bin (right).

The network is trained using MATLAB's *trainnet* function [50] with Adam optimizer [51] and a composite loss function. For each output head, the misfit is measured using the Huber function [52] with threshold δ=0.8 (in natural-log units), which behaves quadratically for small residuals and linearly for large residuals. This choice provides robustness against outliers while retaining sensitivity to small residuals, which is desirable given the heterogeneous quality and recording conditions of strong-motion datasets. Residuals are computed for each period and averaged over the mini-batch, then aggregated across periods. To discourage systematic offsets, we add a bias penalty proportional to the squared mean residual per period, with increased emphasis on the short-period range where prediction uncertainty is largest and engineering sensitivity is highest. Finally, the three component losses are combined with larger weights for the two horizontal components (0.375 each) than for the vertical component (0.25), reflecting their primary importance in most engineering applications. The initial learning rate was set to 5e-4 and it was reducing by half every 40 epochs. To prevent overfitting, early stopping was employed during training. The training data were split into three subsets: (1) a training set (72%), used to calibrate the adjustable ANN weights; (2) a validation set (18%), used to check the validation loss during training and stop the training if the validation loss did not improve for 6 consecutive epochs; and (3) a test set (10%), not used during ANN training and validation, but needed to evaluate the network capability of generalization in the presence of new data.

The main architectural hyperparameters are the widths of the branch-specific layers (N_1) and the shared layer (N_2; see Figure 1). These values were selected through preliminary sensitivity tests to balance predictive performance, training stability, and model parsimony. To keep the number of learnable parameters low while maintaining stable generalization, we set N_1 equal to the number of long-period input ordinates, and N_2 equal to three times the number of short-period output ordinates ensuring sufficient capacity to capture cross-period and cross-component interactions without excessive over-parameterization.

Figure S1 in the Supplemental material 1 illustrates learning curves of ANNs trained using as corner periods 0.7 s and 1~s. The learning curves for both training and validation show a rapid decrease in the composite loss function during the initial epochs, followed by a gradual flattening as the model converges. This suggests that the model rapidly reaches an error floor that is primarily controlled by the information content of the available predictors, rather than by network capacity. In other words, once the principal trends captured by the input variables are learned, the remaining variability in the targets is largely attributable to effects not represented in the feature set (e.g., unmodeled source, path, and site complexity) and to irreducible record-to-record scatter. Under these conditions, increasing the number of neurons or adding additional layers yields only marginal reductions in training and validation loss, resulting in learning curves with limited further improvement after the initial epochs. Moreover, the training and validation losses remain very close throughout, indicating good generalization and no evident overfitting. The selected model corresponds to the epoch with the lowest validation loss.

Additionally, Figure 3 illustrates total residual bars corresponding to ±1 standard deviation (σ) from the predictions of the same ANNs for one horizontal component. Results are presented and compared for the training, validation, and test sets. No bias with period is observed in both cases. Uncertainties clearly increase at shorter periods, i.e., farther from T*. Despite this effect, the prediction accuracy for PGA is generally higher than for short periods. It is worth noting that in both cases, the total σ in ln-units of both the validation and test sets is bounded to ±0.65, which lies at the lower bound of typical total standard deviations reported by recent ground-motion models [53]. This comparatively low dispersion is likely attributable, at least in part, to including long-period SA among the predictors, which adds further constraints and reduces unexplained variability relative to conventional GMMs.

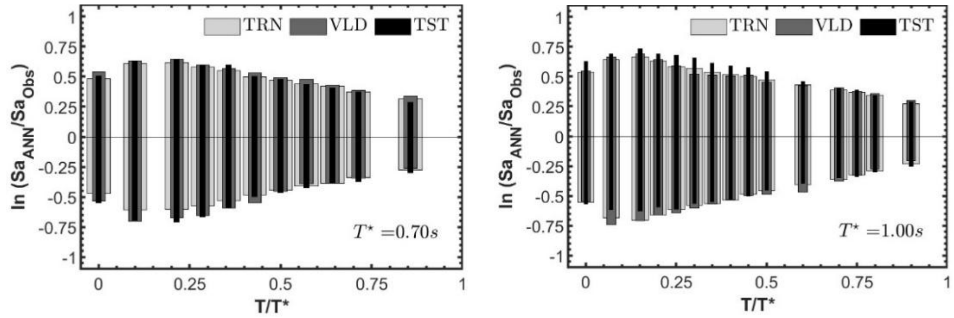

Figure 3. Performance of ANNs trained in predicting SA(T<T*) of the ESM+NGA-West2 data sets, expressed in terms of total logarithmic residuals for one horizontal component, i.e., ln(SA_{ANN}/SA_{Obs}), in which SA_{ANN} denotes the SA predicted by the ANN and SA_{Obs} are the observed ones. The performance is estimated at each vibration period T, here normalized with respect to the corner period T*. The error bars refer to the training (TRN), validation (VLD), and test (TST) sets.

For the ANN with T*=1 s, the Root Mean Squared Error (RMSE) is 0.546, 0.554, and 0.55 for the training, validation, and test sets, respectively, averaged over the three components and all output periods. Other relevant performance metrics are the Mean Absolute Error (MAE), the Coefficient of Determination (R^2), and the linear correlation coefficient (r), which are equal to 0.42, 0.906 and 0.952 for the validation set. Overall, these results indicate good generalization (similar RMSE across training/validation/test) and a strong agreement between predicted and observed short-period spectral ordinates, with most errors within a factor of approximately $e^{0.42} \approx 1.5$ on average.

2.4 Evaluation of physical trends

This section aims at verifying whether the ANN model reproduces key physical ground-motion trends, including attenuation with increasing R_{JB}, and magnitude/near-field saturation. SA estimates are obtained from the model with T*=0.7 s, with long-period input spectra computed from the GMM of Lanzano et al. [53] for the horizontal components, and Ramadan et al. [54] for the vertical one, according to the corresponding fault mechanism, M_w and R_{JB}. This setup allows the physical plausibility of the ANN mapping itself to be examined independently of physics-based simulation variability, by conditioning the model on smooth, well-established median trends.

Figure 4 compares estimated horizontal response spectra from the GMM by Lanzano et al. [53] and from the ANN, for various combinations of M_w and R_{JB}, considering normal faulting, EC8 site class is A, and Italy as region. The spectra show smooth behaviour across the crossover period, with spectral peak shifting systematically to longer periods as M_w increases. Moreover, the agreement is good for magnitudes between 5 and 6.5, while some differences occur at periods around 0.2 s for M_w=7. On the other hand, Figure S2 shows regional differences and the effect of site class. Notably, the ANN estimates for the Taiwan (TW) region are systematically lower than those for other regions, a behaviour that has been consistently observed in empirical studies and is commonly attributed to stronger near-surface attenuation of high frequencies [55].

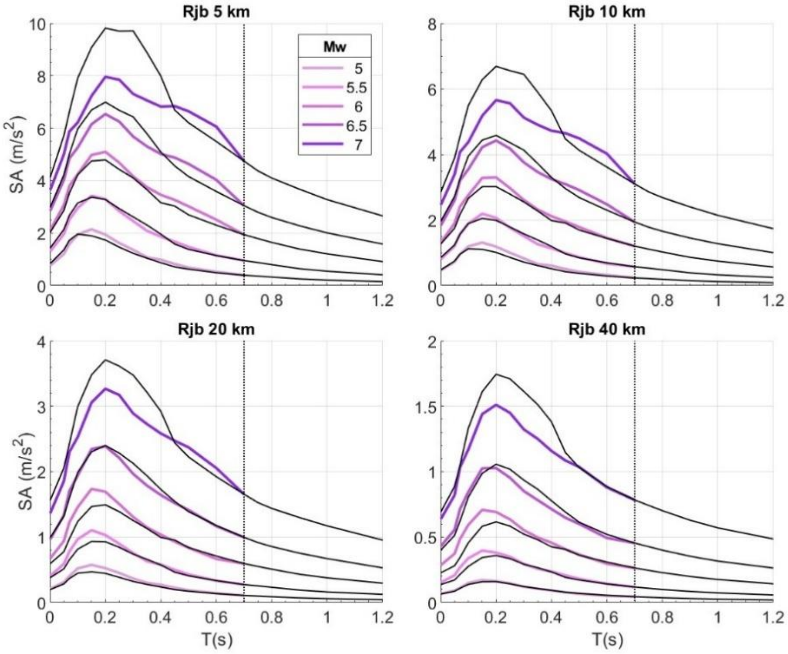

Figure 4. Comparison between estimated horizontal SA from the GMM by Lanzano et al. [53] (black lines), and from the ANN with T*=0.7 s, for different combinations of M_w and R_{JB}, considering normal faulting, SC A, and Italy as region.

Figure 5 shows magnitude and distance scaling for PGA and SA(0.5 s), indicating limited increases beyond about M_w 7 and clear saturation at short distances. The saturation shifts towards larger distances as magnitude increases, reflecting near-field ground-motion saturation, empirically observed in ground motion models. Overall, the artificial neural network model reproduces the key physical trends of ground-motion propagation that are relevant for engineering applications, without introducing evident artefacts or non-physical scaling.

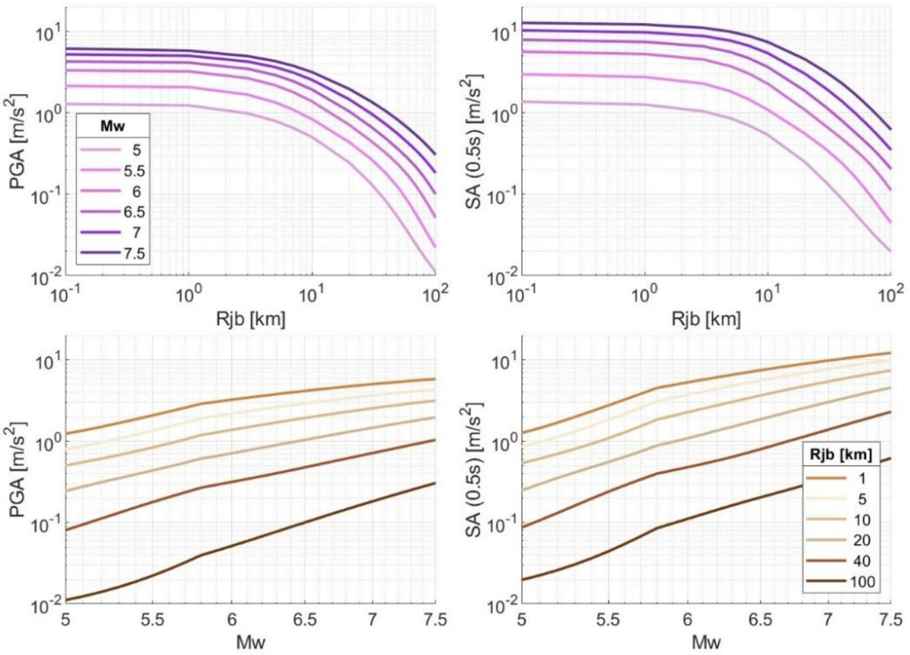

Figure 5. Distance attenuation plots (top) and magnitude saturation (bottom) for PGA and SA(0.5s), estimated from the ANN model with T*=0.7 s, considering reverse faulting, EC8 site class A, and Italy as region.

2.5 Analysis of residuals

Following standard ground-motion decomposition [56], a logarithmic intensity measure (here SA) for event e at site s and period T may be expressed as

$$\ln SA_{es}(T) = \ln \mu_{es}(T) + \delta B_e(T) + \delta W_{es}(T), \tag{2}$$

where $\ln \mu_{es}(T)$ is the median model prediction (here provided by the ANN), $\delta B_e(T)$ is an event term, and $\delta W_{es}(T)$ is the within-event residual. The event terms and within-event residuals are assumed to be uncorrelated and normally distributed with zero mean and standard deviations τ and ϕ, respectively.

We performed a mixed-effects regression on the total residuals separately for each period and component, from which we observed that the within-event standard deviation ϕ decreases systematically with increasing magnitude (see Figure 6), hence, the final mixed-effects regression was performed using a heteroscedastic model for ϕ, defined as

$$\phi(M_w)\begin{cases} \phi_1, & M_w \leq 5, \\ \phi_1 + (M_w - 5)\cdot(\phi_2 - \phi_1), & 5 < M_w < 6, \\ \phi_2, & M_w \geq 6. \end{cases} \tag{3}$$

Within-event standard deviations ϕ_1 and ϕ_2 for all output periods are shown in Figure S3 for the model with T*=1, for one horizontal component and for the vertical component. They vary approximately from 0.3 at periods close to T* and 0.7 at short periods, which is a trend similar to that observed in Figure 3 for the total residuals.

In order to evaluate the validity of our model, we plotted the between-event and within-event residuals against the predictor variables included in the model. Upper panel of Figure 6 shows within-event residuals of one horizontal component at various periods vs R_{JB}, while the lower panel shows their variation with respect to M_w. Figures S4 to S8 show comparisons against other predictor variables. In general, no bias is observed.

Interestingly, the between-event standard deviation τ estimated from the ANN residuals becomes very small and, for several longer periods, effectively vanishes (Figure S3). This occurs because the long-period spectral ordinates provided as inputs capture much of the systematic variability typically attributed to source and path effects (e.g., stress drop, directivity, and attenuation), leaving little coherent event-to-event offset in the residuals once the ANN prediction is removed. At longer periods this conditioning is even more effective, since long-period response is dominated by the coherent, low-frequency source–path content that is well represented by the input spectra; as a result, likelihood-based mixed-effects fits provide no support for an event random effect and the corresponding variance component collapses to the boundary, $\hat{\tau}(T) \approx 0$. Consequently, the remaining unexplained variability at those periods is primarily within-event. This behaviour should not be interpreted as an absence of event-to-event variability in ground motion; rather, it indicates that, conditional on the input spectra, there is little additional event-level structure left to be captured by τ.

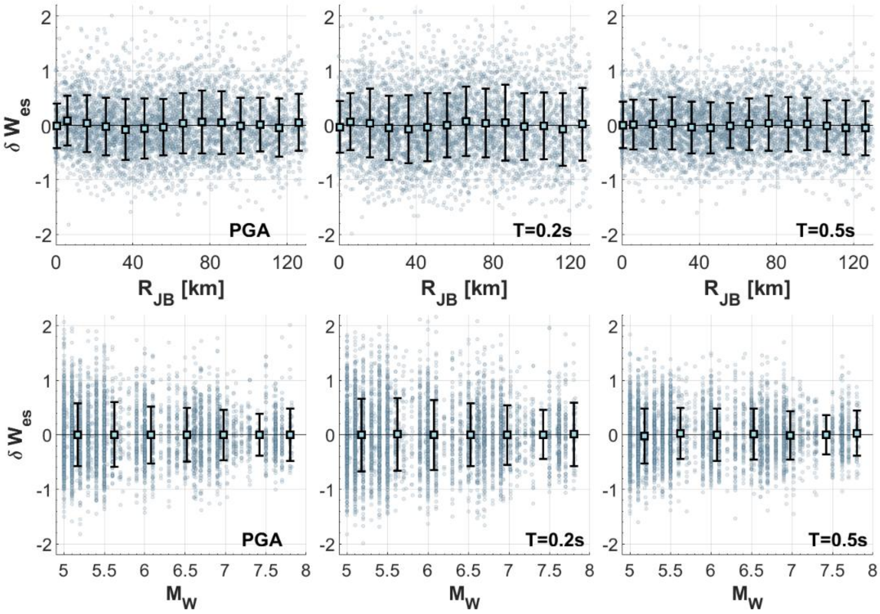

Figure 6. Within-event residuals for a horizontal component at different periods T vs R_{JB} (top panel) and vs M_w (lower panel). Error bars indicate ±1 standard deviation at various bins. T* corresponds to 1 s.

3 Transfer learning

Although the ANN model presented in the previous section incorporates a degree of non-ergodicity by including a dedicated input branch with one-hot encoded region indicators, it is still trained as a single shared model across multiple regions and therefore cannot fully capture region-specific attenuation and near-source scaling characteristics. Because ML models are data-intensive, training a robust ANN using only a limited regional dataset is often impractical and would likely lead to overfitting. To address this limitation, we adopt transfer learning (TL) [32], in which a model pretrained on a larger "source" dataset (or task) is adapted to a smaller "target" dataset (or task). This is implemented here as a two-stage procedure: (1) an ANN is trained on a large ground-motion dataset to learn stable magnitude–distance–site trends; and (2) the early (input and initial hidden) layers are frozen, while the shared and output layers are fine-tuned using regional data. Freezing early layers retains broadly transferable features while allowing the final layers to adjust to local characteristics; combined with early stopping. This strategy improves regional performance while limiting overfitting.

3.1 Application of TL for Iceland

We applied the TL technique to fine-tune the previously developed ANN with T*=1 s, using the Icelandic strong-motion dataset IceSMN [57], consisting of 90 strong-motion tectonic records. This adaptation was motivated by well-documented regional differences in attenuation and near-source scaling in Iceland, whereby commonly used GMMs tend to underpredict short-distance motions and overpredict motions at larger distances [58]. The same distance-dependent bias was observed in the residuals obtained when the original ANN was applied to IceSMN, since the training dataset is a global one, indicating the need for region-specific calibration through fine-tuning.

The surface geology of the South Iceland Lowland results from a combination of volcanic activity, glacial drift, and changes in sea level through the ages. In many areas, sedimentary layers have been covered by layers of basaltic lava and hyaloclastite breccia from the post-glacial period, thus creating soil structures with thin layers of lava rock on top of, or embedded in, unconsolidated sediments [59,60]. This complex near-surface geology makes V_{S30}, and hence EC8 site classes based on V_{S30}, not good predictors of the site response for the unique site conditions in Iceland. Therefore, we decided not to use EC8 site classes as input, as previously done for the global ANN. Based on the work of Darzi et al. [61], we defined four geology-based categories (Figure S9), roughly representing hard rock, soft rock, lava with interbeds and thick soil deposits. These were developed by cross-referencing geological maps with site-to-site residuals (δS22) from the IceSMN dataset with respect to a local GMM. These geology-based categories are given as input in the same way as EC8 site classes, i.e., in encoded form.

It should be noted that while we use site classes as a predictor for site-effects, mostly due to the need for the Iceland case, Vs_{30} could be used as a predictor variable in the fourth branch of the ANN.

Because the transfer-learning stage, in this case, relies on a very limited regional dataset, naïve fine tuning can lead to high-variance updates that overfit period-specific noise rather than physically meaningful spectral trends. With relatively few examples per period, the loss can be reduced by fitting idiosyncratic, sample-specific fluctuations at individual periods rather than learning a smooth spectral shape, which manifests as jagged response spectra with spurious local peaks. To mitigate this effect, we introduce three complementary variance-reduction strategies. First, we apply an L^2-SP regularization term that penalizes deviations of the updated parameters from the pretrained weights [62], thereby anchoring the fine-tuning to physically plausible trends learned from the larger source dataset while allowing only modest regional adjustments. Second, we add a curvature (roughness) penalty on the predicted spectra, implemented via a squared second-difference term across adjacent periods, which directly discourages rapid oscillations in $\ln SA(T)$ and promotes smooth spectral shapes consistent with GMMs. Finally, we use ensemble prediction [63] by training five fine-tuned models with different random split in training/validation/test sets, and averaging their outputs; this reduces prediction variance because idiosyncratic period-to-period fluctuations are not consistent across ensemble members. Together, these measures substantially improve the stability of the fine-tuned spectra without materially altering the underlying mean trends.

Figure 7 presents the within-event residuals as a function of R_{JB} for the transfer-learned ANN (T*=1 s) after fine-tuning on the Icelandic dataset. No systematic distance dependence is evident, indicating that the distance-related bias observed prior to fine-tuning has been effectively mitigated.

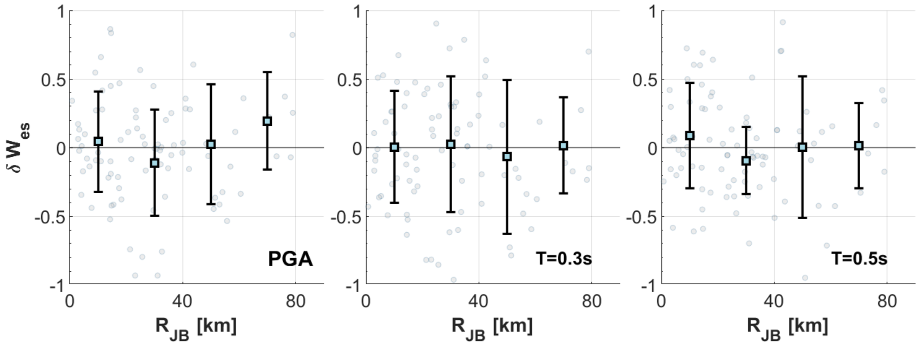

Figure 7. Within-event residuals for a horizontal component at different periods T vs R_{JB}, from an ANN with T*=1 s trained using transfer learning with the Icelandic IceSMN dataset.

4 Spatial and inter-period correlation modelling of within-event residuals

For many earthquake-engineering applications, it is not sufficient to reproduce only the marginal distribution of response spectral ordinates at a site (i.e., median and standard deviation at each period). Scenario-based shaking maps, spatially distributed infrastructure assessments, and portfolio loss calculations are sensitive to the joint behaviour of ground motions across (i) space, (ii) period (or frequency), and often (iii) component. Empirical evidence from recordings shows that within a given event, spectral accelerations at nearby sites tend to deviate from the median in a coherent manner (spatial correlation), and that deviations at different periods are not independent (inter-period correlation). These dependencies can materially affect computed risk metrics, and neglecting them can bias loss and safety estimates [22,25–27].

In this work, correlation modelling focuses on within-event residuals, because they govern the event-specific spatial variability around a median prediction and therefore directly control the spatial coherence of simulated intensity-measure fields. Moreover, as shown earlier, between-event residuals are strongly reduced due the inclusion of long-period spectra as predictor variables. Following Loth and Baker [18] (hereafter LB13), we used normalized within-event residuals obtained from Eq. 2 as

$$\varepsilon(T) = \frac{\delta W_{es}(T)}{\phi(T)} = \frac{\ln SA_{es}(T) - \ln \mu_{es}(T) - \delta B_e(T)}{\phi(T)}. \quad (4)$$

Normalization by the heteroscedastic within-event standard deviation ensures that residuals at different periods and components are placed on a comparable scale prior to correlation modelling. With respect to previous works that focused only on within-event residuals of horizontal (invariant, e.g., RotD50) measures of SA or Fourier spectra [18,24,64], we aim to build a model for the joint dependence of $\varepsilon(T < T*)$ over periods, space and components.

4.1 Geostatistical formulation: covariance and semivariograms

A convenient and widely used geostatistical description of spatial dependence is the cross-semivariogram. For a multivariate residual vector field $\boldsymbol{\varepsilon}(s)$, under assumptions of second-order stationarity and isotropy (dependence only on separation distance h) over the spatial domain considered for a given even, the semivariogram matrix function is defined as

$$\boldsymbol{\Gamma}(h) = \frac{1}{2}\,\mathbb{E}[(\boldsymbol{\varepsilon}(s) - \boldsymbol{\varepsilon}(s+h))(\boldsymbol{\varepsilon}(s) - \boldsymbol{\varepsilon}(s+h))^{\mathrm{T}}], \tag{5}$$

where s represents spatial position. The corresponding covariance matrix function $\mathbf{C}(h)$ satisfies

$$\mathbf{C}(h) = \mathbf{C}(0) - \boldsymbol{\Gamma}(h), \tag{6}$$

so that $\mathbf{C}(0)$ is the co-located covariance across variables (periods and components), while $\mathbf{C}(h)$ for $h > 0$ controls cross-site dependence.

A crucial requirement of any multivariate spatial correlation model is admissibility: for any set of locations $s_1, \dots, s_N$, the full covariance matrix formed by $\mathbf{C}(h_{ij})$ must be positive semidefinite. This requirement is essential for both unconditional simulation and conditional simulation (kriging/conditioning). LB18 emphasize that fitting each period-pair semivariogram independently can lead to covariance matrices that are not positive definite, motivating the use of structured multivariate models that guarantee admissibility by construction. A simple and computationally attractive assumption is separability of $\mathbf{C}(h)$ into a single scalar correlation function $\rho(h)$ governing spatial decay, and a matrix $\mathbf{C}(0)$ capturing inter-period covariance at one site. Separable models guarantee admissibility if $\rho(h)$ is a valid correlation function and $\mathbf{C}(0)$ is positive semidefinite, but they can be overly restrictive. Empirical semivariograms often indicate multiple spatial scales (e.g., a rapid initial increase at small h plus a slower approach to the sill), and the effective range can vary with period. LB18 show that a single-range separable form may not reproduce observed behaviour across all period pairs, and propose nested multiscale models as a practical remedy.

4.2 Linear Model of Coregionalization (LMC)

A standard and flexible multivariate geostatistical model is the Linear Model of Coregionalization (LMC), in which the semivariogram matrix is expressed as a sum of a small number of admissible scalar structures g_ℓ, multiplied by coregionalization matrices $\mathbf{P}^\ell$. The LMC is attractive because admissibility of the resulting covariance is ensured if all coregionalization matrices are positive semidefinite. For ground-motion residuals, both LB13 and Wang et al. [24] (hereafter WO21) adopt a **nested** model with two exponential functions $g_\ell(h) = 1 - \exp(-3h/R)$, plus a nugget. R is known as the correlation length. Using the covariance representation (often more convenient for simulation), a two-range + nugget LMC can be written as

$$\mathbf{C}(h) = \mathbf{P}^1 \exp\left(-\frac{3h}{R_1}\right) + \mathbf{P}^2 \exp\left(-\frac{3h}{R_2}\right) + \mathbf{P}^3\ \mathbb{I}_{\{h=0\}}, \tag{7}$$

where $\mathbf{P}^1$ and $\mathbf{P}^2$ are short- and long-range coregionalization matrices, $\mathbf{P}^3$ is a nugget matrix, and $\mathbb{I}_{\{h=0\}}$ is an indicator function equal to 1 for co-located values and 0 otherwise. R_1 and R_2 are the short- and long-range correlations lengths, respectively. The nugget term produces a discontinuity between $h = 0$ and $h \to 0$, representing micro-scale variability and/or site-specific effects that are not spatially shared between distinct locations. Importantly, the model implies that the co-located covariance is

$$\mathbf{C}(0) = \mathbf{P}^1 + \mathbf{P}^2 + \mathbf{P}^3, \tag{8}$$

which simultaneously defines the inter-period covariance at a single site and, together with the range terms, the cross-site covariance for $h > 0$. This dual role of $h = 0$ and $h > 0$ is emphasized by WO21 and is equally present in the nested LMC used by LB13.

4.3 Empirical estimation and fitting of nested LMC models

The empirical semivariogram matrix is typically computed by binning pairwise differences of within-event residuals by separation distance. Because the aim is to model within-event spatial variability, pairs are formed only from records belonging to the same earthquake, thereby avoiding contamination from between-event effects. LB13 and WO21 both adopt this within-event pairing principle. Denoting by $\Delta\boldsymbol{\varepsilon}_{ij} = \boldsymbol{\varepsilon}(s_i) - \boldsymbol{\varepsilon}(s_j)$ the residual difference vector for a pair of sites with separation h_{ij}, the empirical semivariogram matrix in a distance bin k is

$$\hat{\boldsymbol{\Gamma}}(h_k) = \frac{1}{2n_k}\sum_{(i,j)\in k} \Delta\,\boldsymbol{\varepsilon}_{ij}\;\Delta\boldsymbol{\varepsilon}_{ij}^{\mathrm{T}}, \tag{9}$$

where n_k is the number of pairs in bin k.

To estimate $\mathbf{P}^1$, $\mathbf{P}^2$, $\mathbf{P}^3$ for prescribed ranges R_1, R_2, LB13 use a variant of the Goulard–Voltz $[65]$ iterative algorithm. In essence, for fixed basis functions $g_\ell(h_k)$, the matrices $\mathbf{P}^\ell$are updated by weighted least squares so that the model semivariogram best matches $\hat{\boldsymbol{\Gamma}}(h_k)$ across bins. Weighting is used to stabilize the fit, placing greater emphasis on shorter distances (weights proportional to $1/h_k$). WO21 similarly uses weighted fitting and then enforces positive semidefiniteness through eigenvalue truncation after each update. These steps help ensure the resulting covariance is admissible for simulation.

Because the diagonal of an empirical semivariogram at large distances may not perfectly reach its theoretical sill due to finite sample effects and uneven station geometry, coregionalization matrices can be normalized such that the diagonal terms of $\mathbf{C}(0)$ are equal to one, to maintain consistency with the intended variance and correlation interpretation $[18]$. Hence, the resulting $\mathbf{C}(0)$ is a correlation coefficient model.

4.4 Extension to short-period SAs and three-components

The nested LMC framework is naturally extensible to simultaneously represent inter-period and inter-component dependence. In this work, we model SA(T<T*) for three components simultaneously, hence we stack residuals into a single multivariate field as

$$\boldsymbol{\varepsilon}(s) = [\varepsilon_{H1}(s,T_1),\dots,\varepsilon_{H1}(s,T_{n_P}),\varepsilon_{H2}(s,T_1),\dots,\varepsilon_{H2}(s,T_{n_P}),\varepsilon_v(s,T_1),\dots,\varepsilon_v(s,T_{n_P})]^{\mathrm{T}}, \tag{10}$$

so that $p = 3n_P$ (e.g., n_P=17 for the ANN with T*=1 s). In this form, $\mathbf{C}(0)$ encodes (i) inter-period correlations within a component, (ii) cross-component correlations at the same period, and (iii) cross-component/cross-period correlations, while the spatial ranges R_1, R_2 control how quickly these dependencies decay with distance. This is aligned with the modelling philosophy of LB13, but here it is tailored to the short-period SA range and to multi-component ANN-based broadband prediction.

The two-range + nugget model of Eq. 7 is fitted with $\mathbf{P}^\ell \in \mathbb{R}^{p\times p}$, using the Goulard–Voltz algorithm, with the normalization and weights mentioned in the previous section and used by WO21. In fitting the LMC model we use only residuals from events with more than 20 records, hence, only 3514 from the 5148 records in Figure 2 were used, corresponding to 57 events. Moreover, when fitting the model we do not differentiate by M_w, site or regional classes, since it has been previously shown that although there might be important event-to-event variability in spatial correlation, there is little statistically significant dependence of the spatial [24,66] and inter-period [20,67] correlation on these variables, especially at short periods. We searched iteratively for the optimum (minimum weighted sum of squares - WSS) pair R_1, R_2 in a range close to the values used by WO21 of 10 km 100 km, respectively. For the ANN with T*=1 s, R_1=6 km and R_2=110 km. Figure 8 compares the empirical semivariogram matrix with the fitted nested LMC model for some representative periods for the horizontal component 1 (H1). The same comparison is presented in Figure S10 for the vertical component. These figures demonstrate that the two-range structure captures both the near-field correlation and the decay with separation distance.

Figure 9 shows the co-located covariance matrix C(0). Periods in each block increase from left to right and from top to bottom. First of all, we observe that the diagonal blocks, which represent the inter-period correlations, are very similar for both horizontal components. This was expected since they are as-recorded components and are not aligned to any specific direction with respect to the source. Clearly, if they were aligned to the principal directions [68] or to fault-normal and fault-parallel directions, a different pattern might have been observed. Moreover, we observe that the cross-component correlation between horizontal components is larger than between horizontal and vertical components. For instance, the correlation coefficient between PGA_{H1} and PGA_{H2} is 0.85, while between PGA_{H1} and PGA_V it is 0.74. Finally, the inter-period correlation of horizontal components is slightly larger than for the vertical component.

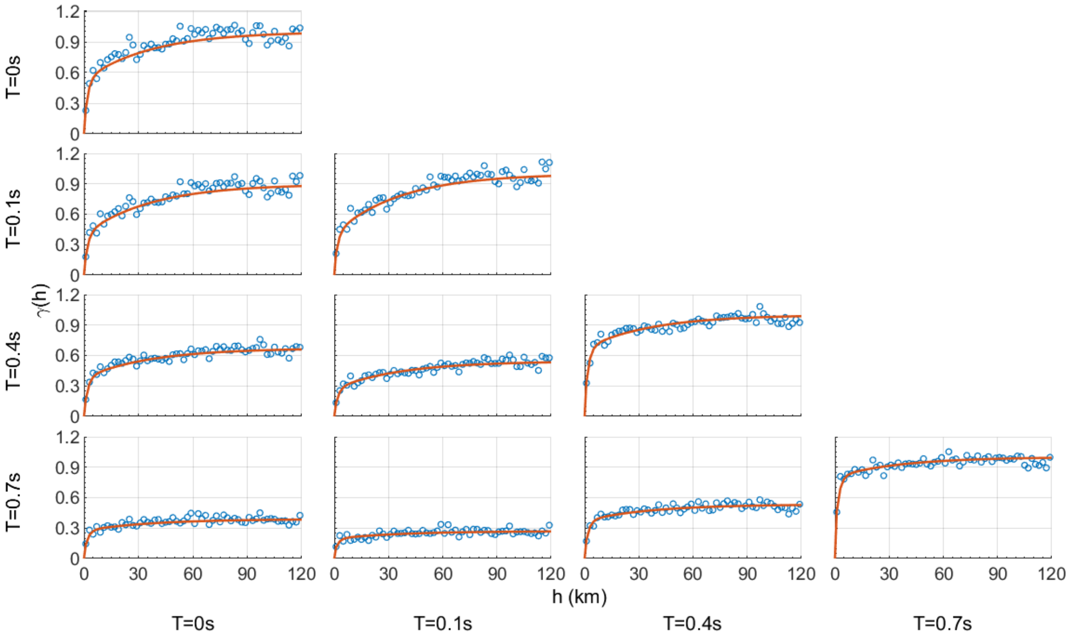

Figure 8. Empirical semivariograms of within-event residuals and the fitted multivariate semivariogram model (solid lines) for horizontal component H1 at period pairs for 0.0, 0.1, 0.4 and 0.7 s. Residuals are computed with respect to the prediction by the ANN with T*=1 s.

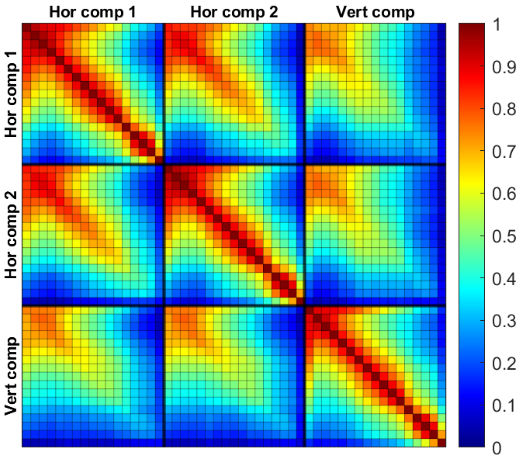

Figure 9. Co-located covariance matrix C(0) in graphical form, indicating the inter-period, cross-component and cross-component/cross-period correlation coefficients. Periods in each block increase from left to right and from top to bottom.

4.5 Simulation of correlated within-event residuals

The fitted covariance model provides the basis for two complementary simulation modes: (i) unconditional simulation, used to generate spatially correlated residual fields for scenario events, and (ii) conditional simulation, used to generate realizations anchored to observed station residuals for reconstructing historical events. In this section we provide a brief description of both simulation methods, which are detailed in Supplemental material 2.

4.5.1 Unconditional simulation

To generate spatially, inter-period, and inter-component correlated short-period residual fields consistent with the fitted nested LMC, we simulate a multivariate, zero-mean Gaussian random field for the normalized within-event residuals $\boldsymbol{\varepsilon}(\mathbf{s}) \in \mathbb{R}^p$, with spatial covariance represented by Eq. 7. Unconditional realizations are obtained by independently simulating the three Gaussian components of the LMC model and summing them, then scaling back to ln-units using the heteroskedastic within-event standard deviations in Eq. 3

$$\boldsymbol{\delta W_{es}} = \boldsymbol{\varepsilon_u}(\mathbf{s}) \odot \boldsymbol{\phi}(\boldsymbol{M_w}), \quad \mathbf{Y}^{\mathrm{sim}}(\mathbf{s}) = \mathbf{Y}^{\mathrm{ANN}}(\mathbf{s}) + \boldsymbol{\delta W_{es}}, \tag{11}$$

where $\odot$ denotes elementwise multiplication, subindex u refers to unconditional simulation, and $\mathbf{Y}^{\mathrm{ANN}}$ are the ANN predictions in ln-units (see Eq. 1).

For large numbers of sites N, the direct approach (forming the full $N \times N$ correlation matrices and applying Cholesky factors) becomes impractical. We therefore optionally replace the exact correlation operators with scalable approximations: a Vecchia/nearest-neighbour approximation for the short-range component [69,70] and a Nyström low-rank approximation for long-range correlations [71].

4.5.2 Conditional simulation

To generate fields conditioned on recorded ground motions at a subset of sites, we implement the "unconditional draw + deterministic conditioning correction" approach described in Hoffman [72]. Given an unconditional realization $\boldsymbol{\varepsilon}_{\boldsymbol{u}}(\mathbf{s})$ obtained as described in Appendix A, the conditioned field of normalized residuals is obtained as

$$\boldsymbol{\varepsilon}_{\boldsymbol{c}}(\mathcal{U}) = \boldsymbol{\varepsilon}_{\boldsymbol{u}}(\mathcal{U}) + \mathbf{C}_{\mathcal{U}\mathcal{O}}\, \mathbf{C}_{\mathcal{O}\mathcal{O}}^{-1}\big(\boldsymbol{\varepsilon}_{\boldsymbol{obs}}(\mathcal{O}) - \boldsymbol{\varepsilon}_{\boldsymbol{u}}(\mathcal{O})\big), \tag{12}$$

where $\mathcal{O}$ and $\mathcal{U}$ are observed and unobserved sites, respectively. This ensures that $\boldsymbol{\varepsilon}_{\boldsymbol{c}}(\mathcal{U})$ are consistent with the observed data, while preserving the spatial correlation structure of the unconditional random field. The simulated field $\mathbf{Y}^{\mathrm{sim}}(\mathbf{s})$ is obtained from Eq. 11 using $\boldsymbol{\varepsilon}_{\boldsymbol{c}}(\mathbf{s})$.

5 Simulation of broadband time histories

Ground motions from PBS are valid only up to a certain frequency $f_{\max}$, dependent on the resolution of the numerical model, however, BB time histories are needed for engineering applications. BB ground motions can be generated as follows

(1) simulation of BB cross-correlated response spectra as described in the previous section;

(2) simulation of a seed non-stationary stochastic (STO) accelerogram per monitor and per component. For the horizontal components we use the method of Sabetta et al. [36], and include coherency between components defined from the model of Hong and Liu [73], while for the vertical component we simulate motions using the model of Cui et al. [74];

(3) STO signals are shifted in time so that the time corresponding to a fixed normalized Arias-intensity level (used as an onset proxy) matches the same time in the PBS signals;

(4) BB signals are created by merging STO signals with the PBS signals in the frequency domain using complementary filters, with a transition band centered at a frequency near but below $f_{\max}$;

(5) the HF part of the BB signals is modified in the frequency domain to match the target BB SA. Since spectral matching can introduce discrepancies in PGA, afterwards we apply a PGA correction similar to the method of Liu et al. [75], which consists in adding/subtracting a high-frequency wavelet at the instance in which PGA occurs;

(6) since spectral matching and the PGA correction can add some drift in displacement, the modified BB signals are merged again with the PBS signals, using the same complementary filters, which ensures that the LF part and any permanent displacement from PBS is retained; and

(7) steps 5 and 6 are repeated until the mismatch between target and BB SA falls below a prescribed threshold.

6 Application case study: South Iceland

In this section we present the results from the application of the proposed broadband generation procedure for two PBS of earthquakes of M_w 6.5 and 6.4 carried out by Hernández-Aguirre et al. [35]. This represents a demanding test case, given the limited frequency content of the physics-based simulations and the sparse strong-motion dataset available for regional calibration. The results presented are not limited to median trends, but we analyze also directionality, inter-period and spatial correlation, which are relevant for seismic hazard and risk applications.

6.1 Physics-based simulations for South Iceland

We use results of regional three-dimensional PBS of seismic wave propagation for the M_w 6.5 and M_w 6.4 June 2000 South Iceland earthquakes generated by [35]. Their numerical model of South Iceland ($138 \times 90 \times 25$ km^3) was developed with a spatial resolution sufficient to propagate frequencies up to $\sim f_{\max}=1.9$ Hz. The seismic rupture process was modelled using a kinematic rupture procedure that incorporates heterogeneous slip, rupture velocity, and peak slip rate as correlated stochastic spatial fields. Results from these simulations are available at 7200 ground surface virtual monitors distributed over the whole domain. For more information about the simulations, we refer the reader to [35], that also discusses the performance of the LF PBS, in comparison with available records, while here we focus on the BB results.

6.2 BB time histories

Times series from the simulations were low-pass filtered at 1.9 Hz, in agreement with the maximum resolvable frequency f_{max}. The filtered PBS signals were subsequently processed using the procedure described in the previous section to generate BB ground motions, using conditional simulation of within-event residuals, anchored on recorded values. The complementary merging filters provide a smooth frequency-domain transition between 1.1 and 1.8 Hz. We emphasize that the corner period of the ANN to be used to estimate short period SA should be higher than $1/f_{max}$, since $SA(1/f_{max})$ is still affected by frequencies larger than f_{max}, which are not present in the PBS signals due to the low-pass filtering. Accordingly, we used T*=1 s, but values slightly lower or higher gave similar results.

Figure 10 compares recorded and simulated BB accelerograms, SA, and Fourier amplitude spectra (FAS) at selected stations for the 17 June 2000 earthquake. The almost perfect fit for SA(T<T*) is due to the conditional simulation used, and any mismatch is due to the spectral matching. We observe an overall good agreement in both, time and frequency domains.

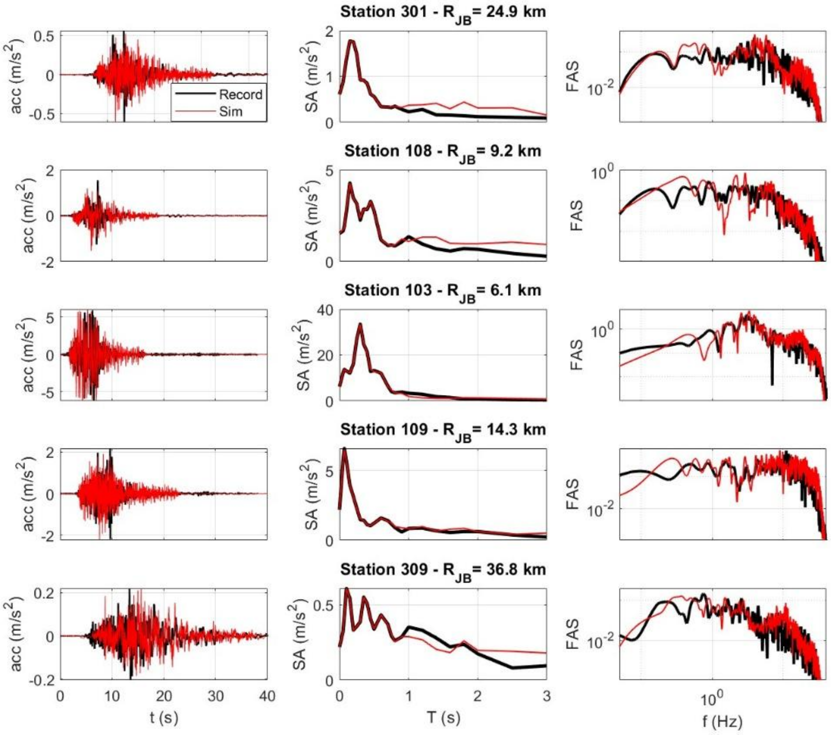

Figure 10. Comparison of recorded and simulated BB accelerograms, SA, and Fourier amplitude spectra (FAS) at selected stations for the 17 June 2000 earthquake.

6.3 Short period attenuation

Figure 11 shows horizontal RotD50 and vertical SA for different short periods as a function of R_{JB}, from recordings (crosses) and simulations (circles). For the horizontal component we also show the estimates of the GMM by Akkar & Bommer (AB10) [76] (yellow lines), and from the local GMM 'F' by Kowsari et al. (KS20) [77] (red lines). SA from KS20 corresponds to a rotational invariant measure, similar to RotD50 [68]. There is currently no ground motion model for vertical SA in Iceland, so we do not show any GMM for that component. The following observations can be made from these comparisons:

- In general, there is a good agreement between records and simulations in terms of attenuation trends with distance across all examined periods;
- The simulated SAs show the expected near-fault saturation in agreement with GMMs;

- Since the GMM KS20 was calibrated using the IceSMN dataset, of which almost half of the records are from the June 2000 South Iceland earthquakes, this model fits very well the recordings and our simulations;
- The GMM by AB10 underestimates SA at short distances and overestimates it further away from the source, which is usually observed from GMMs calibrated from data outside Iceland [58]. This highlights the usefulness of TL, which allows an ANN to be fine-tuned regional data; and
- Vertical SAs have a scatter and attenuation trend very similar to that shown by records.

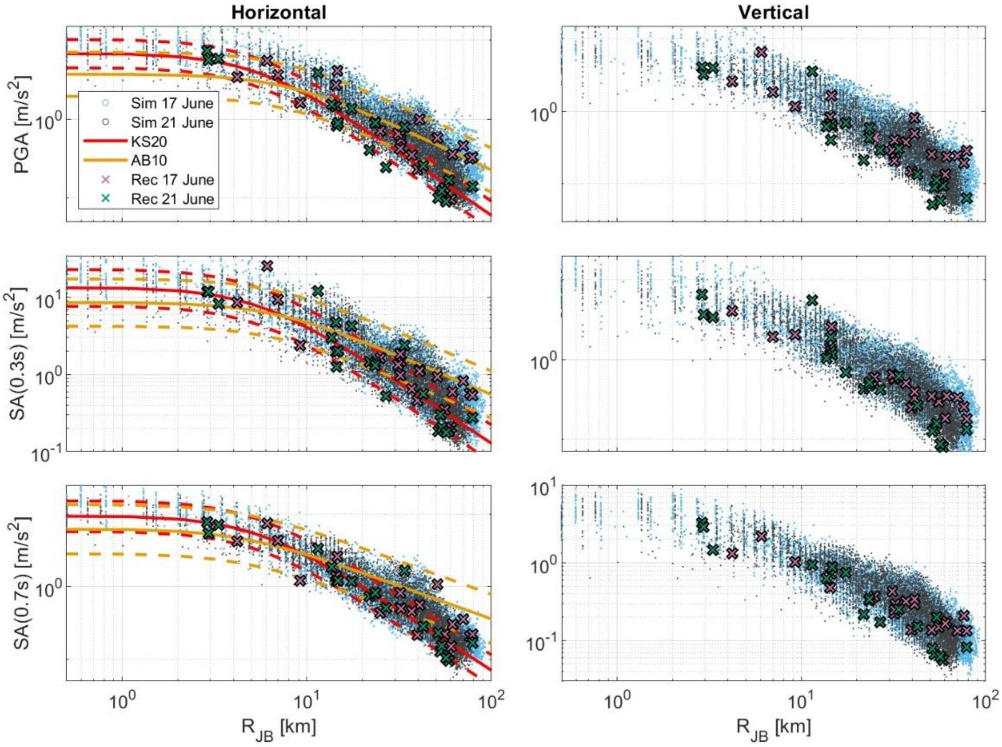

Figure 11. Attenuation of horizontal RotD50 (left) and vertical SA (right) at selected short periods (PGA, 0.3 s and 0.7 s) from recordings (crosses), simulations (circles), and from the GMMs by Akkar & Bommer (AB10) [76] (yellow lines) and Kowsari et al. (KS20) [77] (red lines). Median predictions of the GMMs are shown with solid lines, while median ± one standard deviation are shown with dashed lines.

6.4 Polarization and directionality

Earthquake ground motions display distinctive near-source characteristics [78], such as long-period ground-motion polarization due to rupture directivity and source radiation effects, but such polarization tends to diminish at higher frequencies. Moreover, short-period vertical amplitudes can substantially exceed the horizontal components [79]. By including simultaneously the three components of SA in the ANN, the aim was to preserve physically plausible horizontal polarization and vertical-to-horizontal (V/H) ratios at short periods. In this section we analyse these aspects.

Figure 12 shows maps of fault-normal (FN) PGA, fault-parallel (FP) PGA, and the FN-to-FP PGA ratio for the 21 June 2000 South Iceland earthquake. Although not shown here, the mean FN-to-FP ratios for various short period SAs are very close to one for all distances, which was expected [78]. However, as observed from S11c, there is a clear spatial dependence of this ratio. In the directivity regions, i.e., towards the north and south along the strike direction, the ratio is on average the largest, while in the perpendicular direction it is the lowest. This spatial pattern is consistent with expectations from rupture directivity and S-wave radiation effects, indicating that the short-period motions retain physically meaningful directional characteristics inherited from the long-period physics-based simulations.

The median SARotD100 to SARotD50 ratios at various periods from recordings and simulations are compared to the empirical model of Boore and Kishida (BK2017) [80] in Figure 13a. The recordings show ratios slightly larger than the empirical model at all periods, with a trend against period similar to the model. At periods lower than 0.5 s, controlled by the stochastic part, the ratio from simulations is very close to the empirical model, while in the transition band (~0.6 s to 1 s), where both stochastic and physics-based contributions are present, the ratio increases and gets closer to the ratio from records. In the physics-based dominated part, above 1 s, it is considerably larger than the empirical model, however, it is close what observed from records of both earthquakes.

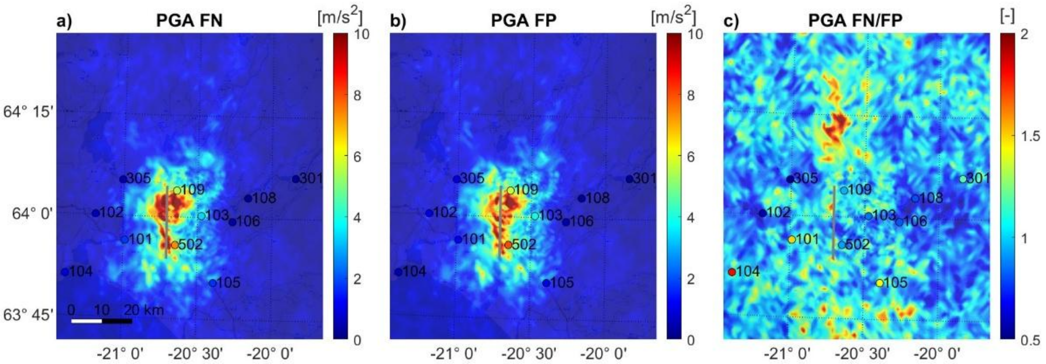

Figure 12. Maps of (a) fault-normal (FN) PGA, (b) fault-parallel (FP) PGA, and (c) FN/FP PGA for the 21 June 2000 South Iceland earthquake. Circles show recorded values using the same colour scale.

Panels b and c of Figure 13 present V/H spectral ratios at two short periods. The horizontal SA are RotD50. Vertical bars denote the mean V/H ratio within discrete distance bins, together with ±1 standard deviation. For comparison, we also plot estimates from the V/H model of Gülerce and Abrahamson (GA2011) [79] for Vs_{30}=760 m/s and a strike-slip event of M_w=6.5. Overall, the simulations are consistent with the empirical model: across all bins, the simulated mean remains within the empirical model median ± one within-event standard deviation. Notably, some locations exhibit V/H ratios exceeding unity, occasionally approaching values close to two. These elevated ratios predominantly occur at locations approximately 45° from the nodal planes of the faulting mechanism, where the S-wave radiation is minimized while the P-wave (producing mostly vertical motion) radiation is maximized, explaining the observed spatial pattern (not shown for brevity).

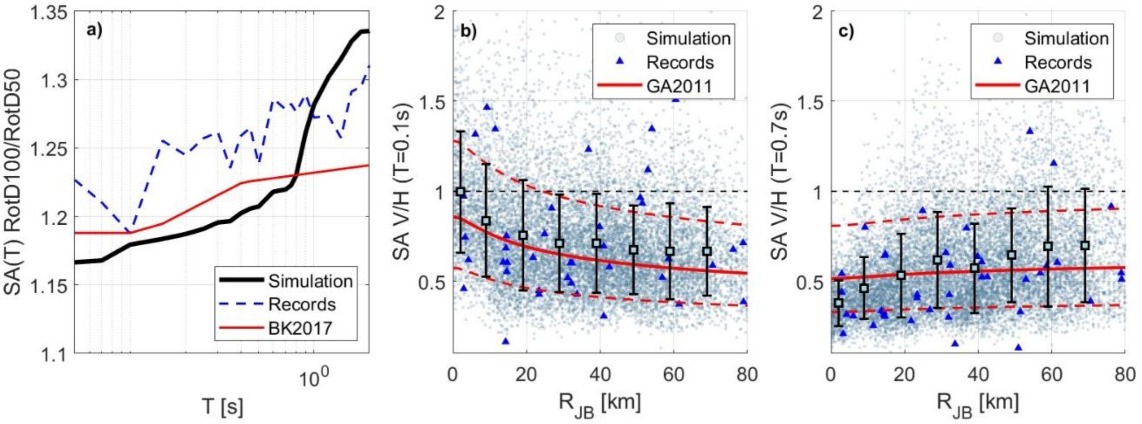

Figure 13. (a) Ratio of SARotD100 to SARotD50 from empirical model of Boore and Kishida (BK2017) [80] and the median ratio from recordings and simulations of the 2000 South Iceland earthquakes. Ratios of vertical to horizontal SA at 0.1 s (b) and 0.7 s (c), from simulations, records, and the model of Gülerce and Abrahamson (GA2011) [79]. The vertical bars represent the mean ± one standard deviation from simulations at various distance bins.

6.5 Inter-period and spatial correlation

Figure 14 shows the correlation coefficients (ρ) between periods T_1 and T_2 of the within-event residuals ε for the two South Iceland earthquakes. Residuals were computed with respect to the local GMM KS20. In general, both simulations follow a trend similar to the empirical model of Baker & Jayaram [21]. The correlation of ε has a smooth transition between the stochastic and physics-based part, indicating that inter-period correlation is preserved across the stochastic–physics-based transition, in contrast to the degradation observed in some earlier hybrid simulation methods [30].

Finally, we computed empirical semivariograms γ(h) from within-event residuals at various periods of the RotD50 SA. Residuals were computed with respect to a simple model fitted to simulated data [29]. Then we fitted an exponential model to the semivariograms using the least squares method. The exponential model is defined as $g(h) = a[1 - \exp(-3h/b)]$, where a is the sill, or the population variance of the random field [81], and b is the range, defined as the inter-site distance at which γ(h) reaches 95% of the sill, beyond which spatial correlation can be considered negligible [15]. Figure 15 shows semivariograms for T=0.1 s and T=0.3 s together with the fitted exponential models. It should be noted that $\gamma(0) \neq 0$, as the LMC model includes a nugget term represented by $\mathbf{P}^3$. This term accounts for spatially uncorrelated variability at infinitesimal separation distances, such as site-specific effects, and results in a non-zero semivariance even at zero lag. Then in panel c we show the estimated ranges at various periods, which are similar to those from empirical models [15,17,82]. Interestingly, the range attains relatively large values around 1 s, which is dominated by the PBS part, potentially reflecting source effects that generate strongly coherent ground motion at those frequencies; however, confirming the physical origin of this behaviour requires further study.

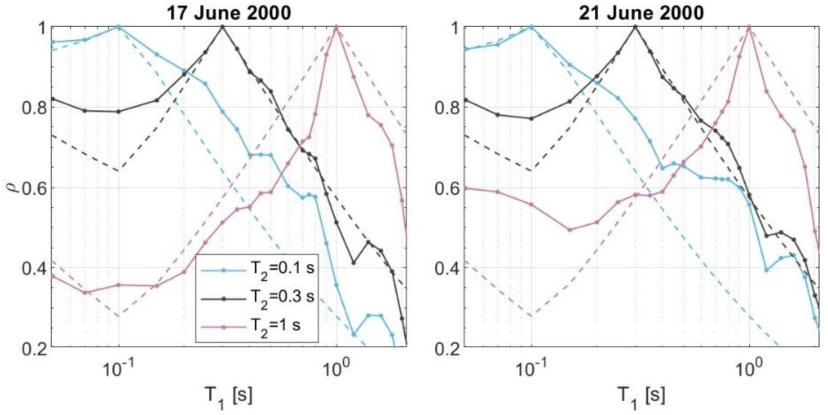

Figure 14. Correlation of ε from simulations of the 2000 South Iceland earthquakes (solid lines), compared with an empirical model (dashed lines) for shallow crustal earthquakes [21], at T_2 =0.1 s, 0.3 s, and 1 s.

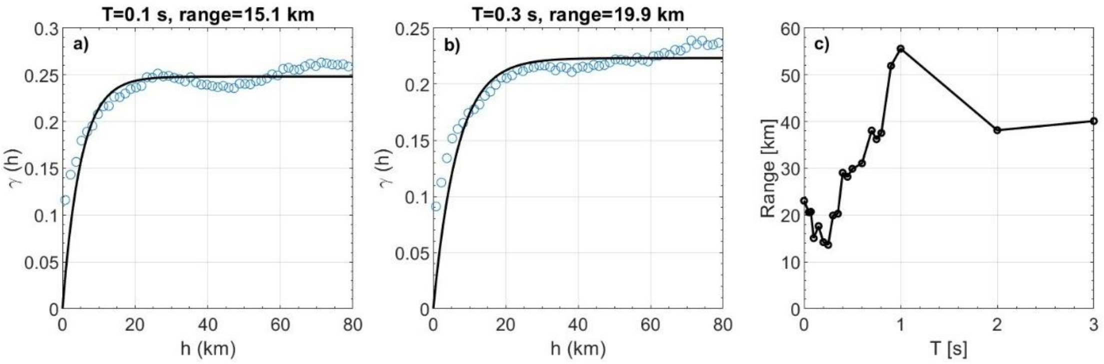

Figure 15. Example empirical semivariograms and fitted exponential models for T=0.1 s (a) and T=0.3 s (b). Spatial correlation ranges estimated for the 21 June 2000 South Iceland simulation (c).

7 Discussion of results

This study presented and validated an enhanced broadband ground-motion generation framework that combines low-frequency PBS, machine-learning predictions of short-period spectral accelerations, and empirically constrained residual correlation modelling~~.~~. The methodology was applied to two different earthquakes in South Iceland, with M_w 6.5–6.4, providing a demanding test case given the limited frequency content of the PBS and the limited ground-motion dataset available to train the ML model.

7.1 Performance of the Broadband Generation Framework

Overall, the proposed workflow yields broadband ground motions that are consistent with observations across multiple dimensions relevant for seismic hazard and risk applications, including amplitude scaling, directionality, and statistical dependence.~~.~~ For the case-study, the attenuation of short-period horizontal and vertical SAs with distance is reproduced realistically, including near-fault saturation effects and realistic scatter. The agreement with the local GMM KS20 is particularly strong, which is expected given that this model was fine-tuned using a dataset dominated by the same earthquake sequence. Importantly, the results also show that TL technique enables the ANN to better represent Icelandic conditions than the same model trained with global data, supporting the use of regional fine-tuning in data-limited environments.

Incorporating additional predictor variables commonly used in NGA-West2–based GMMs [19], such as Z_{TOR}, Z_1, and fault dip, could further enhance the model's predictive performance and potentially reduce aleatory variability. These predictors were not included here because they are not available in the ESM database.

A key methodological aspect is the choice of the transition period T*, which must exceed $1/f_{\max}$ to avoid bias induced by the low-pass filtering of PBS signals. The adopted value T*=1 s for the case study provided stable performance, and the complementary merging filters ensured a smooth blending between stochastic and physics-based contributions without introducing evident spectral discontinuities. If PBS reach higher frequencies, a lower T* could be used.

7.2 Directionality and Component Consistency

Beyond median attenuation trends, the framework preserves physically meaningful directionality and polarization characteristics that are critical for near-fault engineering applications. The spatial patterns of fault-normal and fault-parallel PGA, as well as their ratios, are consistent with expectations from rupture directivity and radiation effects. While average FN/FP ratios at short periods remain close to unity, the spatial variability—particularly elevated ratios in directivity regions—is realistically captured, which is important for near-fault engineering applications.

The RotD100/RotD50 ratios exhibit a coherent transition from stochastic-dominated to physics-dominated regimes. At short periods, simulated ratios track the empirical model of Boore and Kishida [80]; within the transition band they increase toward the levels observed in the recordings; and at longer periods they reflect stronger polarization driven by the PBS, consistent with the data for both earthquakes. Similarly, the vertical-to-horizontal (V/H) ratios align well with the model of Gülerce and Abrahamson [79], including localized exceedances of unity associated with radiation-pattern effects. These results indicate that jointly training the ANN on three components is effective at preserving realistic component-to-component relationships.

7.3 Inter-Period and Spatial Correlation

A central contribution of this work is the explicit and unified treatment of inter-period, spatial and cross-component correlation of within-event residuals. The inter-period correlation structure inferred from simulations closely follows the empirical model of Baker and Jayaram [21], with a smooth transition across the stochastic–physics-based boundary. This behaviour contrasts with earlier hybrid broadband procedures where correlations may degrade near the transition frequency, and suggests that the combined ANN + correlated-residual approach provides a consistent statistical bridge across frequency regimes.

Spatial correlation, assessed via semivariograms of within-event residuals, yields correlation ranges broadly consistent with published empirical models. The presence of a nugget effect is physically plausible and reflects spatially uncorrelated variability (e.g., unresolved site-specific effects and modelling uncertainty), leading to a non-zero semivariance at zero separation. The observation of relatively large correlation ranges around ~1 s is particularly noteworthy and may reflect enhanced source-controlled coherence at intermediate periods for this specific case-study; however, confirming the physical origin of this feature requires additional study.

7.4 Implications for Hazard and Risk Applications

From an engineering perspective, the framework enables the generation of broadband ground-motion fields that are not only spectrally compatible but also statistically consistent across space, periods, and components. This is a key requirement for applications that depend on joint distributions of intensity measures, including vector-valued PSHA, spatially distributed loss estimation, and scenario-based risk analyses for networks and portfolios. Importantly, the approach is computationally efficient: once the ANN is trained, broadband time histories can be generated rapidly for large scenario sets and dense spatial grids.

In addition, the framework provides a practical mechanism to represent aleatory variability in a way that is consistent with observations. Specifically, aleatory uncertainty can be explored by (i) running additional PBS with alternative rupture realizations (e.g., varying slip heterogeneity, rupture velocity, and hypocentre location) to sample source- and path-related variability at long periods, and (ii) generating multiple realizations of the correlated within-event residual field to sample short-period variability and its spatial and cross-period/cross-component dependence. This combination supports the construction of ensembles of broadband ground-motion fields suitable for scenario simulations and probabilistic risk calculations.

Moreover, the approach is particularly attractive in regions with sparse strong-motion data: PBS provides physically constrained long-period motions, while transfer learning and empirically constrained residual correlation provide realistic short-period amplitudes and dependence structures.

7.5 Limitations

Despite the encouraging results, several limitations should be acknowledged.

(i) Reliance on empirical data. The methodology is fundamentally data-driven. Both the ANN predictions at short periods and the residual correlation model depend on empirical strong-motion observations. Consequently, performance may degrade when extrapolating to conditions that are weakly represented in the available datasets (e.g., unusual site conditions, or magnitude–mechanism combinations outside the calibration range). Moreover, the ANN is designed to reproduce statistical trends and variability in intensity measures, rather than to reconstruct a unique physical realization of the short-wavelength field.

(ii) Lack of explicit high-frequency wave propagation physics. High-frequency motion is introduced through stochastic/ML-driven components constrained to match observations, but the framework does not explicitly simulate high-frequency wave propagation (e.g., detailed scattering, small-scale 3-D heterogeneity, and fine-scale site effects). In an ideal setting, fully physics-based broadband simulations would directly propagate energy to high frequencies while simultaneously reproducing realistic spatial and cross-period/cross-component correlations. At present, however, regional PBS are computationally constrained in $f_{\max}$, and achieving both very high frequencies and dependence structures consistent with observations remains challenging. The proposed approach should therefore be viewed as a practical compromise: physics-based where feasible (long periods) and empirically constrained where necessary (short periods and correlation).

(iii) Empirical nature and transferability of the correlation model. The estimated nugget, sill, and range parameters may depend on the region and event characteristics. Applying the same correlation structure outside the calibration context should therefore be done cautiously and preferably supported by additional validation.

(iv) Limited number of validation events. The present application uses two earthquakes in a single region. While this is a relevant and stringent case study, broader testing across additional events, magnitudes, and source–site configurations is needed.

8 Conclusions and Outlook

Within the scope of the South Iceland case study, the proposed broadband generation procedure reproduces observed attenuation trends at short periods, preserves physically plausible directionality and component ratios, and—critically—yields inter-period and spatial correlation structures that are consistent with empirical models and do not exhibit an artificial loss of correlation at the stochastic–PBS transition. These properties make the framework well suited for seismic hazard and risk workflows that require jointly distributed, spatially coherent broadband intensity measures.

Future work should expand validation to additional events and regions, explore sensitivity to PBS configuration and rupture modelling choices, and further investigate the physical mechanisms controlling period-dependent spatial correlation. Moreover, validation could be addressed in terms of engineering demand parameters of elastoplastic single- and multi-degree-of-freedom systems [30,83,84] or in terms of quantitative seismic damage evaluations on building portfolios. Overall, the results indicate that combining physics-based simulations, transfer learning, and empirically constrained correlation modelling offers a robust and practical pathway toward next-generation broadband ground-motion simulation products for seismic hazard and risk assessment.

Acknowledgements

This work was financed by the SERICE project funded by a Grant of Excellence from the Icelandic Centre for Research (RANNIS), Grant Number: 218149-051.

Data Availability Statement Trained ANNs for various corner periods are available at https://github.com/vicmoyhdz/ANN2BB, including training/validation/test sets. The ground motion records used for training the ANN model were obtained the following databases: Engineering Strong-Motion (ESM, https://esm-db.eu/, last accessed November 2025), Pacific Earthquake Engineering Research Center (PEER) NGA-West2 (https://ngawest2.berkeley.edu/, last accessed December 2020).

References

1. McCallen D, Pitarka A, Tang H, et al. Regional-Scale Fault-to-Structure Earthquake Simulations with the EQSIM Framework: Workflow Maturation and Computational Performance on GPU-accelerated Exascale Platforms. *Earthquake Spectra*. 2024;40(3):1615-1652. doi:10.1177/87552930241246235

2. Paolucci R, Mazzieri I, Piunno G, Smerzini C, Vanini M, Özcebe AG. Earthquake Ground Motion Modeling of Induced Seismicity in the Groningen Gas Field. *Earthquake Engineering and Structural Dynamics*. 2021;50(1):135-154. doi:10.1002/eqe.3367
3. Smerzini C, Vanini M, Paolucci R, Renault P, Traversa P. Regional Physics-Based Simulation of Ground Motion within the Rhone Valley, France, during the Mw 4.9 2019 Le Teil Earthquake. *Bulletin of Earthquake Engineering*. 2023;21(4):1747-1774. doi:10.1007/s10518-022-01591-w
4. Hanks TC, McGuire RK. The Character of High-Frequency Strong Ground Motion. *Bulletin of the Seismological Society of America*. 1981;71(6):2071-2095.
5. Motazedian D, Atkinson GM. Stochastic Finite-Fault Modeling Based on a Dynamic Corner Frequency. *Bulletin of the Seismological Society of America*. 2005;95(3):995-1010. doi:10.1785/0120030207
6. Boore DM. Simulation of Ground Motion Using the Stochastic Method. *Pure and Applied Geophysics*. 2003;160(3):635-676. doi:10.1007/PL00012553
7. Douglas J, Aochi H. A Survey of Techniques for Predicting Earthquake Ground Motions for Engineering Purposes. *Surveys in Geophysics*. 2008;29(3):187-220. doi:10.1007/s10712-008-9046-y
8. Graves R, Pitarka A. Broadband ground-motion simulation using a hybrid approach. *Bulletin of the Seismological Society of America*. 2010;100(5 A):2095-2123. doi:10.1785/0120100057
9. Mai PM, Imperatori W, Olsen KB. Hybrid broadband ground-motion simulations: Combining long-period deterministic synthetics with high-frequency multiple s-to-s backscattering. *Bulletin of the Seismological Society of America*. 2010;100(5 A):2124-2142. doi:10.1785/0120080194
10. Olsen K, Takedatsu R. The SDSU Broadband Ground-Motion Generation Module BBtoolbox Version 1.5. *Seismological Research Letters*. 2015;86(1):81-88. doi:10.1785/0220140102
11. Crempien JGF, Archuleta RJ. UCSB Method for Simulation of Broadband Ground Motion from Kinematic Earthquake Sources. *Seismological Research Letters*. 2015;86(1):61-67. doi:10.1785/0220140103
12. Aquib TA, Mai PM. Broadband Ground-Motion Simulations with Machine-Learning-Based High-Frequency Waves from Fourier Neural Operators. *Bulletin of the Seismological Society of America*. 2024;114(6):2846-2868. doi:10.1785/0120240027
13. Gatti F, Clouteau D. Towards Blending Physics-Based Numerical Simulations and Seismic Databases Using Generative Adversarial Network. *Computer Methods in Applied Mechanics and Engineering*. 2020;372. doi:10.1016/j.cma.2020.113421
14. Paolucci R, Gatti F, Infantino M, Smerzini C, Özcebe AG, Stupazzini M. Broadband ground motions from 3D physics-based numerical simulations using artificial neural networks. *Bull Seismol Soc Am*. 2018;108(3):1272-1286. doi:10.1785/0120170293
15. Esposito S, Iervolino I. Spatial Correlation of Spectral Acceleration in European Data. *Bulletin of the Seismological Society of America*. 2012;102(6):2781-2788. doi:10.1785/0120120068
16. Goda K, Hong HP. Spatial Correlation of Peak Ground Motions and Response Spectra. *Bulletin of the Seismological Society of America*. 2008;98(1):354-365. doi:10.1785/0120070078
17. Jayaram N, Baker JW. Correlation model for spatially distributed ground-motion intensities. *Earthq Engng Struct Dyn*. 2009;38(15):1687-1708. doi:10.1002/eqe.922
18. Loth C, Baker JW. A spatial cross-correlation model of spectral accelerations at multiple periods. *Earthq Engng Struct Dyn*. 2013;42(3):397-417. doi:10.1002/eqe.2212
19. Abrahamson NA, Silva WJ, Kamai R. Summary of the ASK14 Ground Motion Relation for Active Crustal Regions. *Earthquake Spectra*. 2014;30(3):1025-1055. doi:10.1193/070913EQS198M
20. Baker JW, Bradley BA. Intensity Measure Correlations Observed in the NGA-West2 Database, and Dependence of Correlations on Rupture and Site Parameters. *Earthquake Spectra*. 2017;33(1):145-156. doi:10.1193/060716eqs095m
21. Baker JW, Jayaram N. Correlation of Spectral Acceleration Values from NGA Ground Motion Models. *Earthquake Spectra*. 2008;24(1):299-317. doi:10.1193/1.2857544
22. Bayless J, Abrahamson NA. Evaluation of the Interperiod Correlation of Ground-Motion Simulations. *Bulletin of the Seismological Society of America*. 2018;108(6):3413-3430. doi:10.1785/0120180095
23. Stafford PJ. Interfrequency Correlations among Fourier Spectral Ordinates and Implications for Stochastic Ground-Motion Simulation. *Bulletin of the Seismological Society of America*. 2017;107(6):2774-2791. doi:10.1785/0120170081
24. Wang N, Olsen KB, Day SM. A Frequency-Dependent Ground-Motion Spatial Correlation Model of within-Event Residuals for Fourier Amplitude Spectra. *Earthquake Spectra*. 2021;37(3):2041-2065. doi:10.1177/8755293020981995

25. Goda K, Atkinson GM. Probabilistic Characterization of Spatially Correlated Response Spectra for Earthquakes in Japan. *Bulletin of the Seismological Society of America*. 2009;99(5):3003-3020. doi:10.1785/0120090007
26. Park J, Bazzurro P, Baker JW. Modeling spatial correlation of ground motion Intensity Measures for regional seismic hazard and portfolio loss estimation. In: *Applications of Statistics and Probability in Civil Engineering*. Taylor & Francis Group, London; 2007.
27. Weatherill GA, Silva V, Crowley H, Bazzurro P. Exploring the impact of spatial correlations and uncertainties for portfolio analysis in probabilistic seismic loss estimation. *Bull Earthquake Eng*. 2015;13(4):957-981. doi:10.1007/s10518-015-9730-5
28. Chen Y, Baker JW. Spatial Correlations in Cybershake Physics-Based Ground-Motion Simulations. *Bulletin of the Seismological Society of America*. 2019;109(6):2447-2458. doi:10.1785/0120190065
29. Infantino M, Smerzini C, Lin J. Spatial Correlation of Broadband Ground Motions from Physics-Based Numerical Simulations. *Earthquake Engineering and Structural Dynamics*. 2021;50(10):2575-2594. doi:10.1002/eqe.3461
30. Burks LS, Baker JW. Validation of Ground-Motion Simulations through Simple Proxies for the Response of Engineered Systems. *Bulletin of the Seismological Society of America*. 2014;104(4):1930-1946. doi:10.1785/0120130276
31. Kubo H, Naoi M, Kano M. Recent advances in earthquake seismology using machine learning. *Earth Planets Space*. 2024;76(1):36. doi:10.1186/s40623-024-01982-0
32. Pan SJ, Yang Q. A Survey on Transfer Learning. *IEEE Transactions on Knowledge and Data Engineering*. 2010;22(10):1345-1359. doi:10.1109/TKDE.2009.191
33. Jozinović D, Lomax A, Štajduhar I, Michelini A. Transfer Learning: Improving Neural Network Based Prediction of Earthquake Ground Shaking for an Area with Insufficient Training Data. *Geophysical Journal International*. 2022;229(1):704-718. doi:10.1093/gji/ggab488
34. Sreenath V, Basu J, Raghukanth STG. Ground Motion Models for Regions with Limited Data: Data-driven Approach. *Earthquake Engineering & Structural Dynamics*. 2024;53(3):1363-1375. doi:10.1002/eqe.4075
35. Hernández-Aguirre VM, Rupakhety R, Paolucci R, Smerzini C, Bessason B, Erlingsson S. A kinematic rupture generator for ground-motion simulations: Validation and scenarios in South Iceland. *Manuscript submitted for publication*. Published online 2026.
36. Sabetta F, Pugliese A, Fiorentino G, Lanzano G, Luzi L. Simulation of Non-Stationary Stochastic Ground Motions Based on Recent Italian Earthquakes. *Bulletin of Earthquake Engineering*. 2021;19(9):3287-3315. doi:10.1007/s10518-021-01077-1
37. Paolucci R, Smerzini C, Vanini M. BB-speedset: A validated dataset of broadband near-source earthquake ground motions from 3d physics-based numerical simulations. *Bulletin of the Seismological Society of America*. 2021;111(5):2527-2545. doi:10.1785/0120210089
38. Sgobba S, Felicetta C, Lanzano G, Ramadan F, D'Amico M, Pacor F. NESS2.0: An Updated Version of the Worldwide Dataset for Calibrating and Adjusting Ground-Motion Models in Near Source. *Bulletin of the Seismological Society of America*. 2021;111(5):2358-2378. doi:10.1785/0120210080
39. Graves R, Pitarka A. Kinematic Ground-Motion Simulations on Rough Faults Including Effects of 3D Stochastic Velocity Perturbations. *Bulletin of the Seismological Society of America*. 2016;106(5):2136-2153. doi:10.1785/0120160088
40. Imperatori W, Mai PM. Broad-band near-field ground motion simulations in 3-dimensional scattering media. *Geophysical Journal International*. 2013;192(2):725-744. doi:10.1093/gji/ggs041
41. Bishop CM. *Neural Networks for Pattern Recognition*. Oxford University Press; 1995. doi:10.1093/oso/9780198538493.001.0001
42. Rumelhart DE, Hinton GE, Williams RJ. Learning representations by back-propagating errors. *Nature*. 1986;323(6088):533-536. doi:10.1038/323533a0
43. Hornik K, Stinchcombe M, White H. Multilayer feedforward networks are universal approximators. *Neural Networks*. 1989;2(5):359-366. doi:https://doi.org/10.1016/0893-6080(89)90020-8
44. Prechelt L. Early stopping — but when? In: Montavon G, Orr GB, Müller KR, eds. *Neural Networks: Tricks of the Trade: Second Edition*. Springer Berlin Heidelberg; 2012:53-67. doi:10.1007/978-3-642-35289-8_5
45. Sharma V, Dhanya J, Gade M, Sivasubramonian J. New Generalized ANN-based Hybrid Broadband Response Spectra Generator Using Physics-based Simulations. *Natural Hazards*. 2023;116(2):1879-1901. doi:10.1007/s11069-022-05746-5

46. Choudhary R, Sharma V, Dhanya J. Hybrid broadband ground motion generator for data-sparse regions. *Georisk: Assessment and Management of Risk for Engineered Systems and Geohazards*. Published online October 9, 2025:1-24. doi:10.1080/17499518.2025.2569548
47. Fayaz J, Xiang Y, Zareian F. Generalized ground motion prediction model using hybrid recurrent neural network. *Earthq Engng Struct Dyn*. 2021;50(6):1539-1561. doi:10.1002/eqe.3410
48. Luzi L, Puglia R, Russo E, et al. The Engineering Strong-Motion Database: A Platform to Access Pan-European Accelerometric Data. *Seismological Research Letters*. 2016;87(4):987-997. doi:10.1785/0220150278
49. Ancheta TD, Darragh RB, Stewart JP, et al. NGA-West2 Database. *Earthquake Spectra*. 2014;30(3):989-1005. doi:10.1193/070913EQS197M
50. The MathWorks Inc. MATLAB version: 24.2 (R2024b). Published online 2024. https://www.mathworks.com
51. Kingma DP, Ba J. Adam: a method for stochastic optimization. In: 2015. doi:https://doi.org/10.48550/arXiv.1412.6980
52. Huber PJ. Robust estimation of a location parameter. In: Kotz S, Johnson NL, eds. *Breakthroughs in Statistics: Methodology and Distribution*. Springer New York; 1992:492-518. doi:10.1007/978-1-4612-4380-9_35
53. Lanzano G, Luzi L, Pacor F, et al. A Revised Ground-Motion Prediction Model for Shallow Crustal Earthquakes in Italy. *Bulletin of the Seismological Society of America*. 2019;109(2):525-540. doi:10.1785/0120180210
54. Ramadan F, Smerzini C, Lanzano G, Pacor F. An Empirical Model for the Vertical-to-Horizontal Spectral Ratios for Italy. *Earthquake Engineering and Structural Dynamics*. 2021;50(15):4121-4141. doi:10.1002/eqe.3548
55. Lin PS, Lee CT, Cheng CT, Sung CH. Response spectral attenuation relations for shallow crustal earthquakes in Taiwan. *Engineering Geology*. 2011;121(3-4):150-164. doi:10.1016/j.enggeo.2011.04.019
56. Al Atik L, Abrahamson N, Bommer JJ, Scherbaum F, Cotton F, Kuehn N. The Variability of Ground-Motion Prediction Models and Its Components. *Seismological Research Letters*. 2010;81(5):794-801. doi:10.1785/gssrl.81.5.794
57. Rupakhety R, Ólafsson S. IceSMN Icelandic Strong Motion Network [Data Set]. *International Federation of Digital Seismograph Networks*. Published online 2015. doi:10.7914/YW8C-NY36
58. Ólafsson S, Sigbjörnsson R. Attenuation in Iceland Compared with Other Regions. In: *First European Conference on Earthquake Engineering and Seismology (1ECEES)*. 2006.
59. Bessason B, Kaynia AM. Site amplification in lava rock on soft sediments. *Soil Dynamics and Earthquake Engineering*. 2002;22(7):525-540. doi:10.1016/S0267-7261(02)00035-0
60. Olafsdottir EA, Erlingsson S, Bessason B. Hybrid non-invasive characterization of soil strata at sites with and without embedded lava rock layers in the South Iceland Seismic Zone. *Bulletin of Engineering Geology and the Environment*. 2023;82(4). doi:10.1007/s10064-023-03136-0
61. Darzi A, Halldorsson B, Cotton F, Rahpeyma S. Nationwide Frequency-Dependent Seismic Site Amplification Models for Iceland. *Soil Dynamics and Earthquake Engineering*. 2024;183. doi:10.1016/j.soildyn.2024.108798
62. Li X, Grandvalet Y, Davoine F. A baseline regularization scheme for transfer learning with convolutional neural networks. *Pattern Recognition*. 2020;98:107049. doi:10.1016/j.patcog.2019.107049
63. Sedaghati F, Pezeshk S. Machine Learning–Based Ground Motion Models for Shallow Crustal Earthquakes in Active Tectonic Regions. *Earthquake Spectra*. 2023;39(4):2406-2435. doi:10.1177/87552930231191759
64. Markhvida M, Ceferino L, Baker JW. Modeling spatially correlated spectral accelerations at multiple periods using principal component analysis and geostatistics. *Earthq Engng Struct Dyn*. 2018;47(5):1107-1123. doi:10.1002/eqe.3007
65. Goulard M, Voltz M. Linear coregionalization model: Tools for estimation and choice of cross-variogram matrix. *Mathematical Geology*. 1992;24(3):269-286. doi:10.1007/BF00893750
66. Heresi P, Miranda E. Uncertainty in intraevent spatial correlation of elastic pseudo-acceleration spectral ordinates. *Bull Earthquake Eng*. 2019;17(3):1099-1115. doi:10.1007/s10518-018-0506-6
67. Bayless J, Abrahamson NA. An Empirical Model for the Interfrequency Correlation of Epsilon for Fourier Amplitude Spectra. *Bulletin of the Seismological Society of America*. 2019;109(3):1058-1070. doi:10.1785/0120180238
68. Rupakhety R, Sigbjörnsson R. Rotation-Invariant Measures of Earthquake Response Spectra. *Bulletin of Earthquake Engineering*. 2013;11(6):1885-1893. doi:10.1007/s10518-013-9472-1

69. Datta A, Banerjee S, Finley AO, Gelfand AE. On nearest-neighbor Gaussian process models for massive spatial data. *WIREs Computational Stats*. 2016;8(5):162-171. doi:10.1002/wics.1383
70. Vecchia AV. Estimation and Model Identification for Continuous Spatial Processes. *Journal of the Royal Statistical Society Series B (Methodological)*. 1988;50(2):297-312.
71. Williams C, Seeger M. Using the nyström method to speed up kernel machines. In: Leen T, Dietterich T, Tresp V, eds. *Advances in Neural Information Processing Systems*. Vol 13. MIT Press; 2000.
72. Hoffman Y. Gaussian fields and constrained simulations of the large-scale structure. In: Martinez VJ, Saar E, Gonzales EM, Pons-Borderia MJ, eds. *Data Analysis in Cosmology*. Springer Berlin Heidelberg; 2009:565-583. doi:10.1007/978-3-540-44767-2_17
73. Hong HP, Liu TJ. Assessment of Coherency for Bidirectional Horizontal Ground Motions and Its Application for Simulating Records at Multiple Stations. *Bulletin of the Seismological Society of America*. 2014;104(5):2491-2502. doi:10.1785/0120130241
74. Cui XZ, Liu YX, Hong HP. A Stochastic Model for Simulating Vertical Pulseless Near-Fault Seismic Ground Motions. *Bulletin of the Seismological Society of America*. 2022;112(2):961-977. doi:10.1785/0120210114
75. Liu P, Jiang X, Li J, Qu H. An improved time-domain spectral matching algorithm for peak adjustment and convergence efficiency optimization. *Soil Dynamics and Earthquake Engineering*. 2025;197:109530. doi:10.1016/j.soildyn.2025.109530
76. Akkar S, Bommer JJ. Empirical equations for the prediction of PGA, PGV, and spectral accelerations in Europe, the mediterranean region, and the Middle East. *Seismological Research Letters*. 2010;81(2):195-206. doi:10.1785/gssrl.81.2.195
77. Kowsari M, Sonnemann T, Halldorsson B, Hrafnkelsson B, Snæbjörnsson J, Jónsson S. Bayesian inference of empirical ground motion models to pseudo-spectral accelerations of south Iceland seismic zone earthquakes based on informative priors. *Soil Dynamics and Earthquake Engineering*. 2020;132. doi:10.1016/j.soildyn.2020.106075
78. Somerville PG, Smith NF, Graves RW, Services WCF, Abrahamson NA. Modification of Empirical Strong Ground Motion Attenuation Relations to Include the Amplitude and Duration Effects of Rupture Directivity. *Seismological Research Letters*. 1997;68(1):199-222.
79. Gülerce Z, Abrahamson NA. Site-Specific Design Spectra for Vertical Ground Motion. *Earthquake Spectra*. 2011;27(4):1023-1047. doi:10.1193/1.3651317
80. Boore DM, Kishida T. Relations between Some Horizontal-Component Ground-Motion Intensity Measures Used in Practice. *Bulletin of the Seismological Society of America*. 2017;107(1):334-343. doi:10.1785/0120160250
81. Barnes RJ. The variogram sill and the sample variance. *Mathematical Geology*. 1991;23(4):673-678. doi:10.1007/BF02065813
82. Huang C, Galasso C. Ground-motion intensity measure correlations observed in Italian strong-motion records. *Earthq Engng Struct Dyn*. 2019;48(15):1634-1660. doi:10.1002/eqe.3216
83. Galasso C, Zhong P, Zareian F, Iervolino I, Graves RW. Validation of ground-motion simulations for historical events using MDoF systems. *Earthq Engng Struct Dyn*. 2013;42(9):1395-1412. doi:10.1002/eqe.2278
84. Smerzini C, Amendola C, Paolucci R, Bazrafshan A. Engineering Validation of BB-SPEEDset, a Data Set of near-Source Physics-Based Simulated Accelerograms. *Earthquake Spectra*. 2024;40(1):420-445. doi:10.1177/87552930231206766

Electronic supplement 1

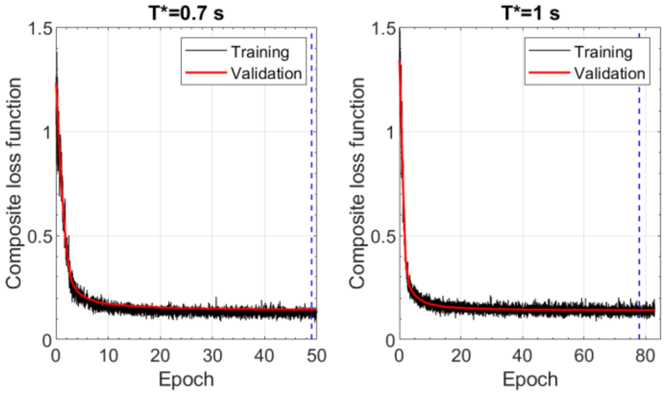

Figure S 1. Learning curves for ANNs trained using as corner period T*=0.7 s (left), and T*=1 s (right). The blue dashed lines represent the epoch with the lowest validation loss which is the one selected.

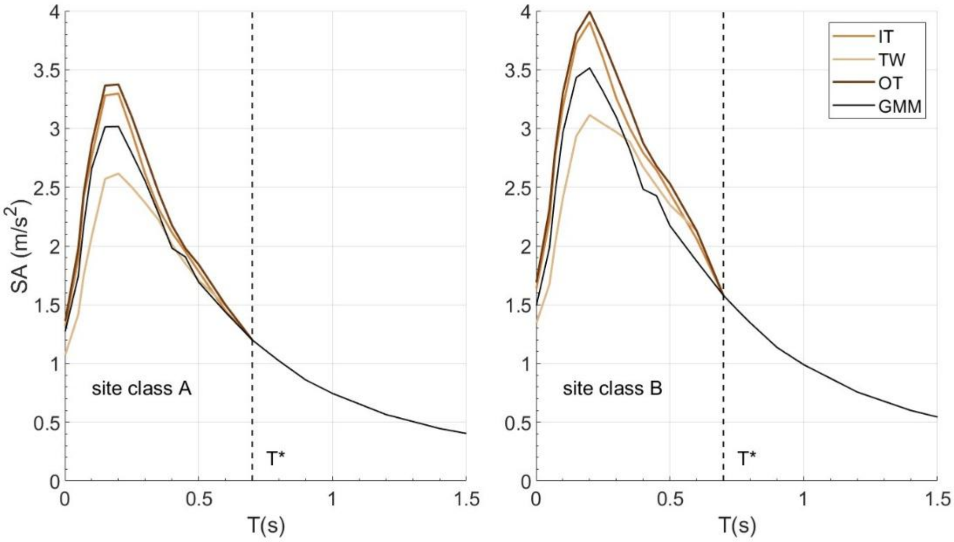

Figure S 2. Comparison of estimated horizontal response spectra for different regions by the ANN with T*=0.7 s. The source mechanism is normal faulting, $M_W=6$ and $R_{JB}=10$ km. EC8 site class is A on the left and B on the right. The input long-period spectra were obtained from the GMM by Lanzano et al. (2019).

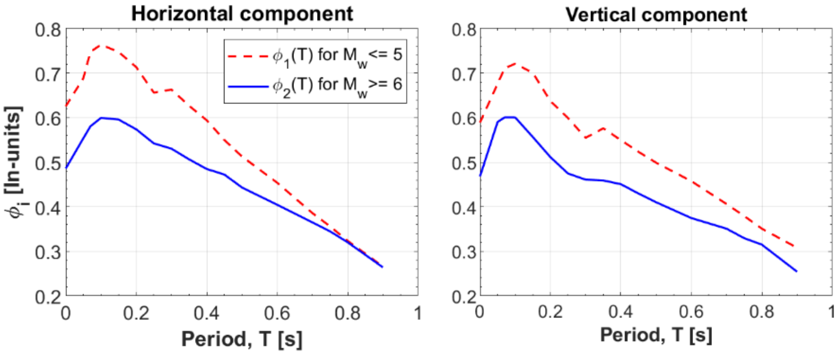

Figure S 3. Within-event standard deviations ϕ_1 and ϕ_2 from the heteroscedastic mixed-effects regression for all output periods for the ANN with T*=1 s.

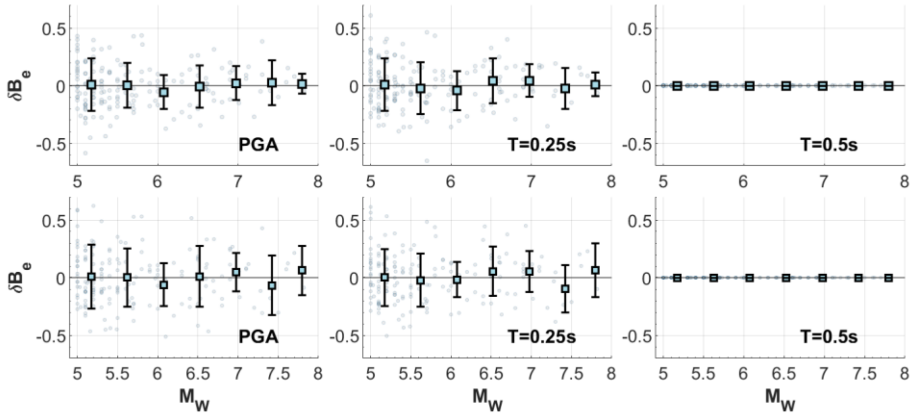

Figure S 4. Between-event residuals at various periods vs M$_w$ for one horizontal component (top panel) and for the vertical component (lower panel). Error bars indicate ±1 standard deviation at various bins. T* corresponds to 1 s.

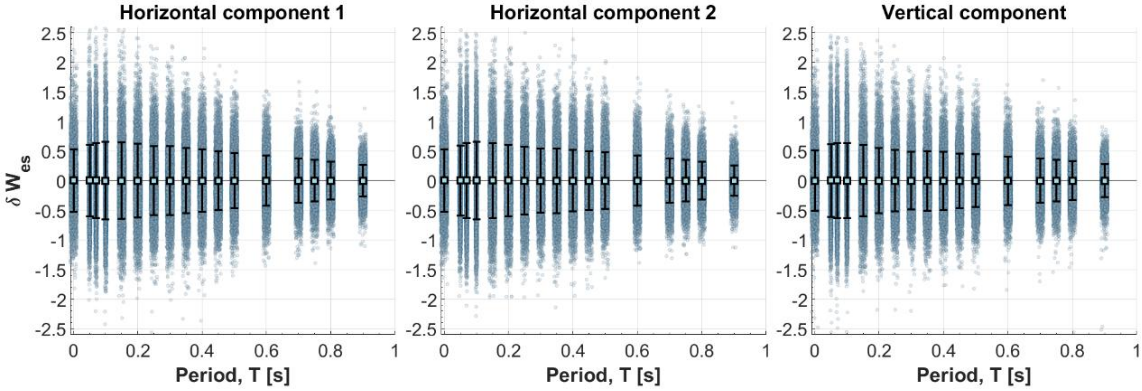

Figure S 5. Within-event residuals vs period for the three components. Points are plotted with a small horizontal jitter to reduce overlap and improve readability. Error bars indicate ±1 standard deviation. T* corresponds to 1 s. T* corresponds to 1 s.

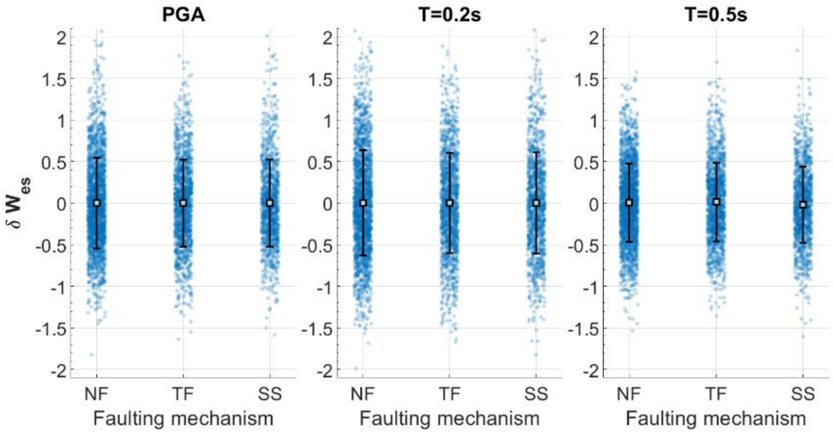

Figure S 6. Within-event residuals at various periods vs faulting mechanism for one horizontal component. Points are plotted with a small horizontal jitter to reduce overlap and improve readability. Error bars indicate ±1 standard deviation. T* corresponds to 1 s.

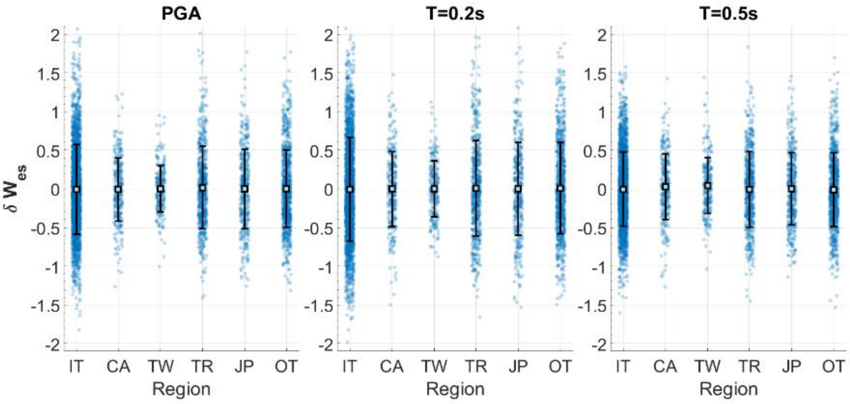

Figure S 7. Within-event residuals at various periods vs region for one horizontal component. Points are plotted with a small horizontal jitter to reduce overlap and improve readability. Error bars indicate ±1 standard deviation. T* corresponds to 1 s.

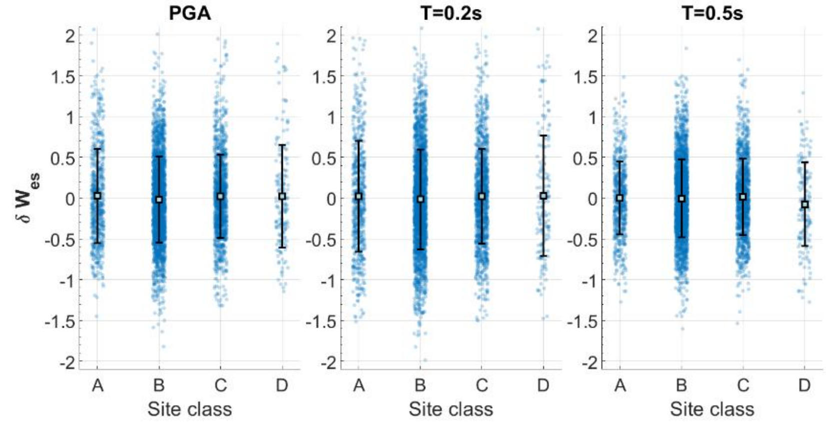

Figure S 8. Within-event residuals at various periods vs EC8 site class for one horizontal component. Points are plotted with a small horizontal jitter to reduce overlap and improve readability. Error bars indicate ±1 standard deviation. T* corresponds to 1 s.

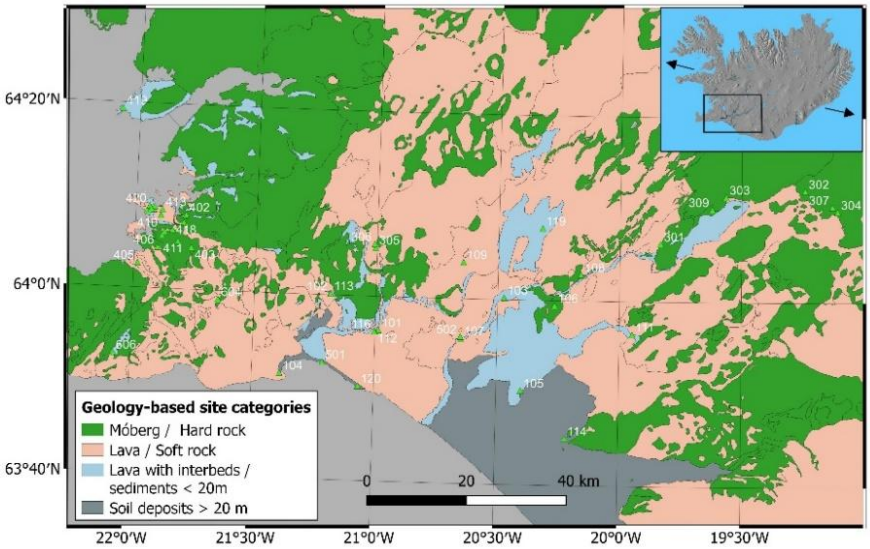

Figure S 9. Geology-based site classes used for training the ANN for Iceland.

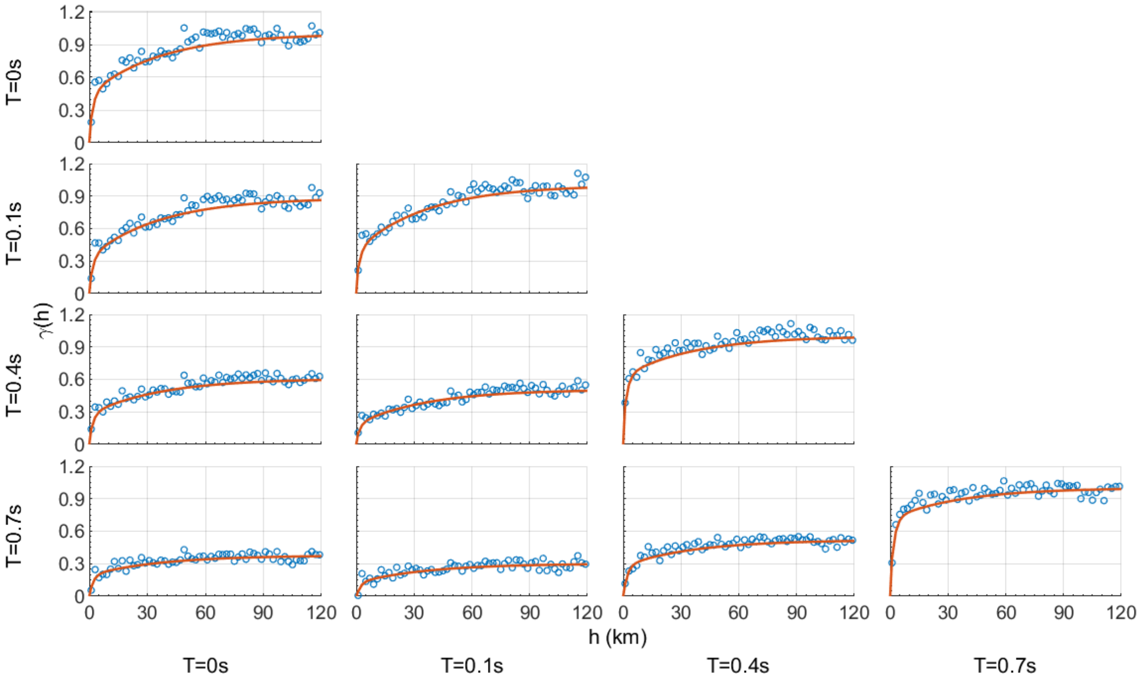

Figure S 10. Empirical semivariograms of within-event residuals and the fitted multivariate semivariogram model (solid lines) for the vertical component at period pairs for 0.0, 0.1, 0.4 and 0.7 s. Residuals are computed with respect to the prediction by the ANN with T*=1 s.

Electronic supplement 2

Simulation of multivariate LMC residual fields

A.1. Random field definition and stacking

Let $\mathbf{s} \in \mathbb{R}^2$denote a site coordinate (e.g., UTM in km). We simulate a multivariate Gaussian random field for the normalized within-event residuals,

$$\boldsymbol{\varepsilon}(\mathbf{s}) = \begin{bmatrix} \boldsymbol{\varepsilon}^{H1}(\mathbf{s}) \\ \boldsymbol{\varepsilon}^{H2}(\mathbf{s}) \\ \boldsymbol{\varepsilon}^{V}(\mathbf{s}) \end{bmatrix} \in \mathbb{R}^p, p = 3n_P, \tag{A1}$$

where each block $\boldsymbol{\varepsilon}^{\boldsymbol{comp}}(\mathbf{s}) \in \mathbb{R}^{n_P}$ corresponds to the set of short-period ordinates (all periods simulated simultaneously). The normalized residuals are defined by period/component-specific heteroscedastic within-event standard deviations $\boldsymbol{\phi}(\boldsymbol{M_w}) \in \mathbb{R}^p$ estimated from mixed-effects residual decomposition. Following the nested LMC structure used in spatial cross-correlation modeling (Loth and Baker 2013) and consistent with the frequency-dependent formulation of Wang et al. (2021), we represent the covariance of $\boldsymbol{\varepsilon}(\mathbf{s})$ as a sum of two spatially correlated components with exponential correlation functions and a nugget component, defined by Eq. 7.

A.2. Direct unconditional simulation

For a set of N sites $\{\mathbf{s}_i\}_{i=1}^N$, define the $N \times N$ distance matrix H with entries $H_{ij} = h_{ij} = \| \mathbf{s}_i - \mathbf{s}_j \|$. The two spatial correlation matrices are

$$\mathbf{R}_1 = \left[exp\left(\frac{-3h_{ij}}{R_1}\right)\right]_{i,j=1}^N, \mathbf{R}_2 = \left[exp\left(\frac{-3h_{ij}}{R_2}\right)\right]_{i,j=1}^N. \tag{A2}$$

In the direct implementation, we compute Cholesky factors $\mathbf{L}_\ell \mathbf{L}_\ell^\top \approx \mathbf{R}_\ell$ with a small jitter added to ensure positive definiteness. Likewise, we factor the coregionalization matrices $\mathbf{P}_\ell$ into $\mathbf{B}_\ell \mathbf{B}_\ell^\top$ (using PSD projection if needed). We then simulate three independent Gaussian components using matrix-normal algebra:

$$\boldsymbol{\varepsilon}_1 = (\mathbf{B}_1\, \mathbf{Z}_1\, \mathbf{L}_1^\top)^\top, \boldsymbol{\varepsilon}_2 = (\mathbf{B}_2\, \mathbf{Z}_2\, \mathbf{L}_2^\top)^\top, \boldsymbol{\varepsilon}_3 = (\mathbf{B}_3\, \mathbf{Z}_3)^\top, \tag{A3}$$

where $\mathbf{Z}_1, \mathbf{Z}_2, \mathbf{Z}_3 \in \mathbb{R}^{d \times N}$ have i.i.d. standard normal entries. The resulting unconditional normalized field is

$$\boldsymbol{\varepsilon} = \boldsymbol{\varepsilon}_1 + \boldsymbol{\varepsilon}_2 + \boldsymbol{\varepsilon}_3 \in \mathbb{R}^{N \times p}, \tag{A4}$$

with covariance

$$\mathrm{Cov}[\mathrm{vec}(\boldsymbol{\varepsilon})] = \mathbf{P}_1 \otimes \mathbf{R}_1 + \mathbf{P}_2 \otimes \mathbf{R}_2 + \mathbf{P}_3 \otimes \mathbf{I}_N, \tag{A5}$$

where $\otimes$ denotes the Kronecker product and $\mathrm{vec}(\cdot)$ stacks by columns.

Because the subsequent step exponentiates simulated ln-fields back to linear spectral accelerations, extreme Gaussian tails can occasionally yield unrealistically large amplitudes when N is large. As a practical safeguard, we optionally apply a smooth saturation to the normalized field (Winsorization-like):

$$\tilde{\boldsymbol{\varepsilon}} = c \tan\mathrm{h}(\boldsymbol{\varepsilon}/c), \tag{A6}$$

with c set to 2. Finally, the simulated residuals in ln-units are obtained by rescaling with $\boldsymbol{\phi}(\boldsymbol{M_w})$:

$$\boldsymbol{\delta W_{es}} = \tilde{\boldsymbol{\varepsilon}} \odot \boldsymbol{\phi}, \quad \mathbf{Y}^{\mathrm{sim}} = \mathbf{Y}^{\mathrm{ANN}} + \boldsymbol{\delta W_{es}}, \tag{A7}$$

where $\mathbf{Y}^{\mathrm{ANN}} \in \mathbb{R}^{N \times d}$contains the ANN mean predictions ln-units.

A.4. Scalable simulation for large N: Vecchia and Nyström approximations

The direct approach requires storing dense $N \times N$ matrices and performing $O(N^3)$ Cholesky factorization, which becomes infeasible for $N \sim 10^4$–10^5. We therefore implement scalable approximations of the correlation operators:

Short-range (Vecchia / nearest-neighbour): For the short-range component $\mathbf{R}_1$, we approximate the joint distribution by a product of low-dimensional conditionals (Vecchia, 1988). In modern form, this yields sparse precision and triangular factors that enable simulation with cost $O(Nm^2)$, where m is the neighbour set size (Datta et al., 2016). This approximation is well suited for rapidly decaying correlations.

Long-range (Nyström low-rank): For long-range correlations $\mathbf{R}_2$, we approximate $\mathbf{R}_2$by a low-rank factorization based on $m \ll N$ landmark points (Williams & Seeger, 2000),

$$\mathbf{R}_2 \approx \mathbf{U}\mathbf{U}^{\top}, \tag{A8}$$

so that a correlated draw can be generated as $\mathbf{r} \approx \mathbf{U}\mathbf{z}$ with $\mathbf{z} \sim \mathcal{N}(\mathbf{0}, \mathbf{I}_m)$. This reduces memory and computation while preserving the dominant long-range modes. In practice, we combine the short- and long-range approximations in a hybrid manner consistent with the additive LMC decomposition as in Eq. A4.

A.5. Conditional simulation by deterministic correction

To condition simulated fields on recorded spectral accelerations, we follow the "unconditional draw + deterministic conditioning correction" method described by Hoffman (2009) for conditional random fields. Let $\mathcal{O}$ be the set of observation indices (size N_o) and $\mathcal{U}$ the set of unobserved sites (size N_u). Given recorded values at $\mathcal{O}$, we compute observed normalized within-event residuals relative to the ANN prediction as

$$\boldsymbol{\varepsilon}_{\text{obs}}(\mathcal{O}) = \left(\mathbf{Y}^{\text{obs}}(\mathcal{O}) - \mathbf{Y}^{\text{ANN}}(\mathcal{O})\right) \oslash \boldsymbol{\phi}(\boldsymbol{M}_w), \tag{A9}$$

where $\oslash$ represents elementwise division. We first generate an unconditional normalized field at all sites $\boldsymbol{\varepsilon}_u(\boldsymbol{s} = \mathcal{O} \cup \mathcal{U})$ as described before. Define the mismatch at observed sites as

$$\Delta(\mathcal{O}) = \boldsymbol{\varepsilon}_{\text{obs}}(\mathcal{O}) - \boldsymbol{\varepsilon}_u(\mathcal{O}). \tag{A10}$$

The conditioned field is then obtained by adding the kriging-like correction term,

$$\boldsymbol{\varepsilon}_c(\mathcal{U}) = \boldsymbol{\varepsilon}_u(\mathcal{U}) + \mathbf{C}_{\mathcal{U}\mathcal{O}}\,\mathbf{C}_{\mathcal{O}\mathcal{O}}^{-1}\,\Delta(\mathcal{O}), \tag{A11}$$

where $\mathbf{C}_{\mathcal{O}\mathcal{O}}$ is the block covariance among observed sites and $\mathbf{C}_{\mathcal{U}\mathcal{O}}$ is the cross-covariance between unobserved sites and observed sites. Under the nested LMC covariance above, and using the nugget convention, these blocks take the form

◦

$$\mathbf{C}_{\mathcal{O}\mathcal{O}} = \mathbf{P}_1 \otimes \mathbf{R}_{oo}^{(1)} + \mathbf{P}_2 \otimes \mathbf{R}_{oo}^{(2)} + \mathbf{P}_3 \otimes \mathbf{I}_{N_o}, \tag{A12}$$

$$\mathbf{C}_{\mathcal{U}\mathcal{O}} = \mathbf{P}_1 \otimes \mathbf{R}_{uo}^{(1)} + \mathbf{P}_2 \otimes \mathbf{R}_{uo}^{(2)}, \tag{A13}$$

where $\mathbf{R}_{oo}^{(\ell)}$ and $\mathbf{R}_{uo}^{(\ell)}$ are exponential correlation matrices computed from observation–observation and unobserved–observation distances for range R_ℓ, computed as in Eq. A2 The nugget $\mathbf{P}_3$ appears only in $\mathbf{C}_{\mathcal{O}\mathcal{O}}$ (variance at the same site), and not in $\mathbf{C}_{\mathcal{U}\mathcal{O}}$, consistent with independent nugget contributions across distinct sites.

A.6. Practical computation of $\boldsymbol{C}_{\mathcal{U}\mathcal{O}}\mathbf{C}_{\mathcal{O}\mathcal{O}}^{-1}\boldsymbol{\Delta}(\boldsymbol{\mathcal{O}})$

Directly forming and inverting $C_{\mathcal{O}\mathcal{O}}$ might be computationally expensive if N_o is large, moreover, the full matrix $\mathbf{C}_{\mathcal{U}\mathcal{O}}$ is usually very large. Instead, we compute the product $\mathbf{C}_{\mathcal{U}\mathcal{O}}\mathbf{C}_{\mathcal{O}\mathcal{O}}^{-1}\Delta(\mathcal{O})$ in two stages:

We first solve the linear system

$$\boldsymbol{C}_{\mathcal{O}\mathcal{O}} vec(\alpha^T) = vec(\Delta(\mathcal{O})^T), \tag{A14}$$

where $\alpha \in R^{N_o \times d}$ is an auxiliary matrix of "kriging weights" (one d-vector per observed site), and $vec(\cdot)$ stacks the columns of its argument. This equation makes the Kronecker structure explicit and fixes the ordering used in implementation. In practice we compute $vec(\alpha^T)$ by a Cholesky factorization of $\boldsymbol{C}_{\mathcal{O}\mathcal{O}}$. Specifically, we form an upper-triangular factor U such that $\boldsymbol{C}_{\mathcal{O}\mathcal{O}} \approx U^T U$, and then apply two triangular solves

$$U^T z = vec(\Delta(\mathcal{O})^T), Uvec(\alpha^T) = z. \tag{A15}$$

A small diagonal stabilization (jitter) may be added to $\boldsymbol{C}_{\mathcal{OO}}$ if needed for numerical robustness. After solving for $vec(\alpha^T)$, we reshape to obtain α in site-major form.

Once α is known, the correction at the unobserved locations is computed using matrix multiplications that avoid forming the full $(N_u d) \times (N_o d)$ matrix $\boldsymbol{C}_{\mathcal{UO}}$. Using the LMC decomposition,

$$\boldsymbol{C}_{\mathcal{UO}} \boldsymbol{C}_{\mathcal{OO}}^{-1} \Delta(\mathcal{O}) = \left(\boldsymbol{P}_1 \otimes \boldsymbol{R}_{uo}^{(1)} + \boldsymbol{P}_2 \otimes \boldsymbol{R}_{uo}^{(2)}\right) vec(\alpha^T). \tag{A16}$$

With the site-major representation $\alpha \in R^{N_o \times d}$, this product can be evaluated as

$$Adj(\mathcal{U}) = \left(\boldsymbol{R}_{uo}^{(1)} \alpha\right) \boldsymbol{P}_1{}^T + \left(\boldsymbol{R}_{uo}^{(2)} \alpha\right) \boldsymbol{P}_2{}^T, \tag{A17}$$

where $Adj(\mathcal{U}) \in R^{N_u \times d}$ is the deterministic correction added to the unconditional field. Finally,

$$\boldsymbol{\varepsilon}_c(\mathcal{U}) = \boldsymbol{\varepsilon}_u(\mathcal{U}) + Adj(\mathcal{U}). \tag{A18}$$

This two-stage computation is exactly what is implemented in the code: (i) solve a single linear system of size $N_o d$ to obtain α, and (ii) apply the cross-covariances from the unobserved points to the observed points through two dense multiplications $\boldsymbol{R}_{uo}^{(\ell)} \alpha$ followed by right-multiplication by P_ℓ^T. Finally, the conditioned ln-residual field and simulated ln-SAs are computed using Eq. A7.